

3-D radial gravity gradient inversion

Vanderlei C. Oliveira Jr. and Valéria C.F. Barbosa

Observatório Nacional, Gal. José Cristino, 77, São Cristóvão, Rio de Janeiro 20921-400, Brazil. E-mail: vandscoelho@gmail.com

Accepted 2013 July 29. Received 2013 July 24; in original form 2013 January 1

SUMMARY

We have presented a joint inversion of all gravity-gradient tensor components to estimate the shape of an isolated 3-D geological body located in subsurface. The method assumes the knowledge about the depth to the top and density contrast of the source. The geological body is approximated by an interpretation model formed by an ensemble of vertically juxtaposed 3-D right prisms, each one with known thickness and density contrast. All prisms forming the interpretation model have a polygonal horizontal cross-section that approximates a depth slice of the body. Each polygon defining a horizontal cross-section has the same fixed number of vertices, which are equally spaced from 0° to 360° and have their horizontal locations described in polar coordinates referred to an arbitrary origin inside the polygon. Although the number of vertices forming each polygon is known, the horizontal coordinates of these vertices are unknown. To retrieve a set of juxtaposed depth slices of the body, and consequently, its shape, our method estimates the radii of all vertices and the horizontal Cartesian coordinates of all arbitrary origins defining the geometry of all polygons describing the horizontal cross-sections of the prisms forming the interpretation model. To obtain a stable estimate that fits the observed data, we impose constraints on the shape of the estimated body. These constraints are imposed through the well-known zeroth- and first-order Tikhonov regularizations allowing, for example, the estimate of vertical or dipping bodies. If the data do not have enough in-depth resolution, the proposed inverse method can obtain a set of stable estimates fitting the observed data with different maximum depths. To analyse the data resolution and deal with this possible ambiguity, we plot the ℓ_2 -norm of the residuals (s) against the estimated volume (v_p) produced by a set of estimated sources having different maximum depths. If this $s \times v_p$ curve (s as a function of v_p) shows a well-defined minimum of s , the data have enough resolution to recover the shape of the body entirely. Conversely, if the observed data do not have enough resolution, some estimates with different maximum depths produce practically the same minimum value of s on the $s \times v_p$ curve. In this case, the best estimate among a suite of estimates producing equally data fits is the one fitting the gravity-gradient data and producing the minima of both the source's bottom depth and volume. The histograms of the residuals can be used to quantify and remove systematic errors in the data. After removing these errors, we confirmed the ability of our method to recover the source geometry entirely (or its upper part only), if the data have sufficient (or insufficient) in-depth resolution. By inverting the gravity-gradient data from a survey over the Vinton salt dome (Louisiana, USA) with a density contrast of 0.55 g cm^{-3} , we estimated a massive cap rock whose maximum depth attains $460 \pm 10 \text{ m}$ and its shallowest portion is elongated in the northeast–southwest direction.

Key words: Numerical solutions; Inverse theory; Numerical approximations and analysis; Gravity anomalies and Earth structure.

1 INTRODUCTION

The vertical component of the gravity field has long been used to retrieve the shape of 3-D (or 2-D) geological sources. Two approaches for the reconstruction of bodies from vertical component of the gravity anomaly have usually been adopted.

The first and most straightforward approach adopts the interactive gravity forward modelling (e.g. Oezsen 2004; Caratori-Tontini *et al.*

2009; Gordon *et al.* 2012). This first approach has frequently been used to interpret multiple anomalous sources with complex shapes and closely separated (either vertically and laterally) from each other by short distances.

The second approach to obtain the shape of anomalous sources is based on linear or non-linear gravity inversion. This approach can be used to directly estimate either the density-contrast distribution or the geometry of the anomalous sources. Many gravity-inversion

methods have been developed for estimating density-contrast distribution and some examples are given in Last & Kubik (1983), Guillen & Menichetti (1984), Barbosa & Silva (1994), Li & Oldenburg (1998), Portniaguine & Zhdanov (1999), Bertete-Aguirre *et al.* (2002), Silva & Barbosa (2006), Farquharson (2008), Lelièvre & Oldenburg (2009), Silva Dias *et al.* (2009), Fregoso & Gallardo (2009) and Silva Dias *et al.* (2011). In these gravity-inversion methods, the Earth's subsurface is discretized into a grid of cubic cells (2-D or 3-D) and the density-contrast distribution is estimated to retrieve the sources' shapes. Other class of gravity-inversion methods to retrieve the shape of anomalous sources estimates a set of geometric parameters which approximates the anomalous source shape. Usually, these gravity-inversion methods assume the knowledge about the density contrast and may be grouped into two categories. The first one estimates the depths to a lower (or upper) boundary of a geological body by assuming the knowledge of the other one boundary estimates, while the second category estimates the coordinates of the boundary surface entirely enclosing a geological body. Most of gravity-inversion methods in the first category have been developed to produce depth-to-basement estimates. Examples for depth-to-basement estimation include the spectral and non-spectral inversion methods (see Barbosa & Silva 2011 for a complete review). The spectral inversion methods for depth-to-basement estimation use the Parker's (1973) forward method to rapidly compute the potential field anomaly of an arbitrary interface separating two homogeneous media. By assuming the knowledge about the average depth of the basement, Guspi (1993) followed spectral inversion to successfully obtain the depth-to-basement estimates for a variety of density contrasts. The non-spectral inversion methods for depth-to-basement estimation discretize the sedimentary pack into a regular grid of rectangular prisms with prescribed densities, fixed tops and unknown thicknesses which represent the depths to the basement. Examples of successful inversion of gravity data to estimate basement relief by using non-spectral information are given in Richardson & MacInnes (1989), Barbosa *et al.* (1997, 1999), Silva *et al.* (2006), Martins *et al.* (2010, 2011) and Silva *et al.* (2010). The methods belonging to this category gave rise to plethora of gravity-inversion algorithms. Conversely, the second category that retrieves the shape of geological sources by estimating the coordinates of the boundary surface entirely enclosing a geological body has led to few gravity-inversion methods (e.g. Silva *et al.* 2000; Moraes & Hansen 2001; Silva & Barbosa 2004; Wildman & Gazonas 2009; Luo 2010; Oliveira Jr. *et al.* 2011).

Recently, gravity-gradient data have been used to interpret 3-D (or 2-D) geological sources. Some interpretation methods using gravity-gradient data follow a well-known automatic aeromagnetic interpretation method called Euler deconvolution. These gravity-gradient interpretation methods are suitable to locate the depth and horizontal positions of geological bodies. Zhang *et al.* (2000) modified the conventional Euler deconvolution method for gravity tensor gradient data. Other examples of gravity-gradient interpretation methods in this direction are based on eigenvectors of the gravity tensor and on Euler deconvolution (e.g. Mikhailov *et al.* 2007; Beiki & Pedersen 2010).

More recently, few gravity-gradient data inversions have been developed not only to locate but also to delineate geological bodies. To date, most of the available gradient-inversion methods estimate a 3-D density-contrast distribution by assuming a piecewise constant function defined on a user-specified grid of cells (e.g. Li 2001; Zhdanov *et al.* 2004). Such methods demand large amount of prior information about the source; otherwise, the inversion produces a rough image of the source distribution whose maximum and

minimum estimated values occur at the boundary of the discretized region. Besides, the linear gravity-gradient inversions for estimating a 3-D density-contrast distribution have the disadvantage of dealing with intractable large-scale 3-D inversion with hundreds of thousands of parameters and tens of thousands of data. This disadvantage requires computational strategies to handle with large amount of computer memory and processing time, like that proposed by Uieda & Barbosa (2012). These authors fix the value of some user-specified cells (named seeds) and propagate its physical properties to adjacent cells in an iterative growing scheme.

To our knowledge, few published methods solve a non-linear gravity-gradient data inversion to retrieve the shape of an anomalous source by estimating a set of geometric parameters which approximates the anomalous source shape. In the 2-D case, this non-linear inversion is proposed by Ditmar (2002). In the 3-D case, Barnes & Barraud (2012) estimate the upper surface of salt bodies by incorporating the total variation regularization and depth estimates from the interpretation of 2-D seismic. However, there is as yet no non-linear inversion of gravity-gradient data that estimates the 3-D boundary surface enclosing the geological body entirely. This paper follows this latter non-linear inversion of gravity-gradient data. Specifically, we adopted the same strategy used in Oliveira Jr. *et al.* (2011), the so-called *Radial Inversion*. This non-linear inversion of gravity-gradient data eliminates most of the above-mentioned disadvantages of linear inversion methods for estimating a 3-D density-contrast distribution. Like Oliveira Jr. *et al.* (2011), we approximate the 3-D source by a set of vertically stacked right prisms with known thicknesses and density contrasts. Each prism has a polygonal horizontal cross-section whose vertices are described by polar coordinates referred to an origin within the polygon. The horizontal Cartesian coordinates of this origin and the radii of the vertices describing the horizontal cross-sections of all prisms are the parameters to be estimated by the non-linear joint inversion of all gravity-gradient tensor components. We used a wide variety of regularizing constraints to obtain stable solutions. Here, we developed a new criterion for analyzing the data resolution and determining the estimate having both the optimum depth to the bottom and the optimum volume. Our criterion is based on the curve between the volume and the ℓ_2 -norm of the data-misfit produced by a set of estimated sources with different tentative maximum depths. The mathematical approach used here differs from that used by Oliveira Jr. *et al.* (2011) and makes it feasible to be applied to multiple potential-field data sets. Finally, tests on synthetic gravity-gradient data and on field data collected over the Vinton salt dome, southwest Louisiana, USA, confirm the potential of our approach.

2 METHODOLOGY

Let $\mathbf{g}^{\alpha\beta}$ the $N^{\alpha\beta}$ -dimensional vector whose i th element is the $\alpha\beta$ -component $g_i^{\alpha\beta}$ of the gravity-gradient tensor (grey scale maps in the upper part of Fig. 1a) measured at the point (x_i, y_i, z_i) . Let us assume that these $N^{\alpha\beta}$ observed gravity-gradient data are produced by a 3-D outcropping source (or a buried source, but with a known depth to the top at z_0) confined beneath the Earth's surface (dark grey volume in the lower part of Fig. 1a). We assume that the density contrast ρ between the geological source and the host rocks is either constant or variable along the vertical direction. To obtain the 3-D source shape, we approximate the volume of the source by a set of L vertically juxtaposed 3-D prisms (light grey prisms, identified by P^k , $k = 1, \dots, L$, in Fig. 1a), like Oliveira Jr. *et al.* (2011). The density contrast of each prism, ρ^k , $k = 1, \dots, L$, is assumed constant and known. Each prism has a constant and known

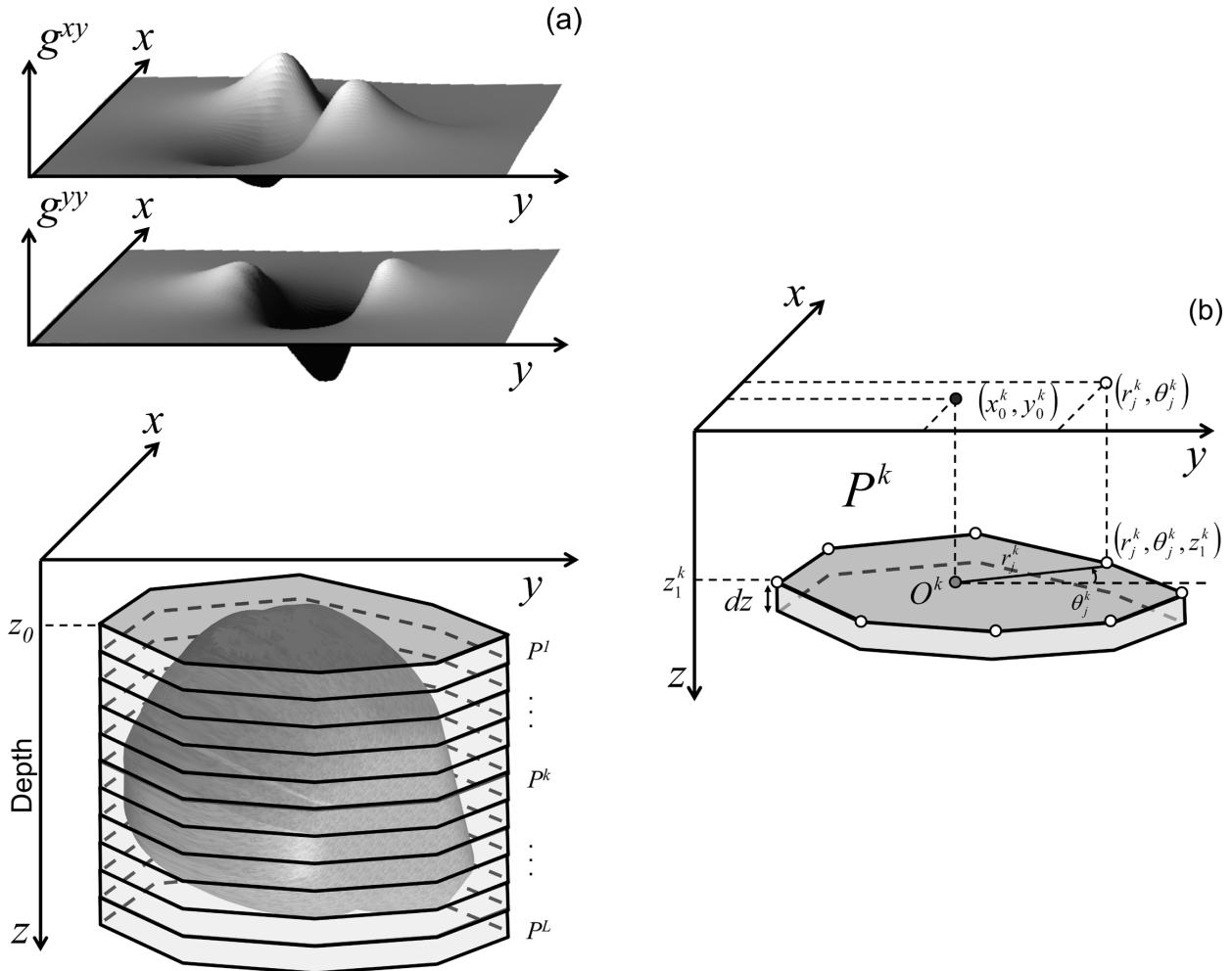


Figure 1. Schematic representation of the interpretation model. (a) Observed g^{xy} and g^{yy} components of the gravity gradient tensor (grey scale maps) produced by the 3-D source (dark grey volume) limited by the closed surface S . The interpretation model is formed by L juxtaposed prisms P^k , $k = 1, \dots, L$, (light grey). (b) The k th prism P^k with thickness dz and M^k vertices described by polar coordinates (r_j^k, θ_j^k) , $j = 1, \dots, M^k$, $k = 1, \dots, L$ (white dots), referred to an arbitrary origin O^k (grey dot) with horizontal Cartesian coordinates x_0^k and y_0^k (black dot).

thickness dz and a horizontal cross-section described by a polygon with a fixed number M^k , $k = 1, \dots, L$, of vertices (white dots in Fig. 1b) equally spaced from 0° to 360° , whose sides approximately describe the edges of horizontal depth slices of the source. The vertices of the polygon are described in polar coordinates referred to an arbitrary origin O^k (grey dot in Fig. 1b) within the polygon. The radii of the vertices $(r_j^k, j = 1, \dots, M^k, k = 1, \dots, L)$ and the horizontal Cartesian coordinates $(x_0^k, y_0^k, k = 1, \dots, L)$ of the arbitrary origins O^k , $k = 1, \dots, L$, of the ensemble of the L vertically stacked prisms are arranged in the M -dimensional vector \mathbf{m} , $M = 2L + \sum_{k=1}^L M^k$, which will be estimated from the observed gravity-gradient data set. For convenience, we used the same number of vertices M^k , $k = 1, \dots, L$, for all prisms forming the interpretation model.

The observed data $g_i^{\alpha\beta}$ can be approximated by the sum of the gravitational effect predicted by the L vertically stacked 3-D prisms (light grey prisms in Fig. 1a) setting up the interpretation model, that is:

$$d_i^{\alpha\beta}(\mathbf{m}) \equiv \sum_{k=1}^L f_i^{\alpha\beta}(\mathbf{r}^k, x_0^k, y_0^k, \boldsymbol{\theta}^k, \rho^k, z_1^k, dz), \quad i = 1, \dots, N^{\alpha\beta}, \quad (1)$$

where \mathbf{r}^k and $\boldsymbol{\theta}^k$ are the M^k -dimensional vectors containing, respectively, the radii r_j^k and angular coordinates $\theta_j^k = (j-1)2\pi/M^k$, $j = 1, \dots, M^k$, $k = 1, \dots, L$, of the k th prism's vertices (Fig. 1b). The non-linear function $f_i^{\alpha\beta}(\mathbf{r}^k, x_0^k, y_0^k, \boldsymbol{\theta}^k, \rho^k, z_1^k, dz)$ is based on Plouff (1976, eq. 9) to calculate the predicted $\alpha\beta$ -component of the gravity-gradient tensor, at the i th observation point (x_i, y_i, z_i) , produced by the k th prism P^k (Fig. 1b), which has the depth to the top given by $z_1^k = z_0 + (k-1)dz$.

Let $\psi^{\alpha\beta}(\mathbf{m})$ be the data-misfit function which measures the squared ℓ_2 -norm of the difference between the observed and predicted $\alpha\beta$ -component of the gravity gradient tensor, that is,

$$\psi^{\alpha\beta}(\mathbf{m}) = \frac{w^{\alpha\beta}}{N^{\alpha\beta}} \|\mathbf{d}^{\alpha\beta}(\mathbf{m}) - \mathbf{g}^{\alpha\beta}\|_2^2, \quad (2)$$

where $\mathbf{d}^{\alpha\beta}(\mathbf{m})$ is the $N^{\alpha\beta}$ -dimensional vector whose i th element $d_i^{\alpha\beta}$ is given by eq. (1) and $w^{\alpha\beta}$ is a normalizing factor defined as

$$w^{\alpha\beta} = \frac{\sqrt{N^{\alpha\beta}}}{\|\mathbf{g}^{\alpha\beta}\|_2}. \quad (3)$$

The role of these weights (eq. 3) is to deal with data sets with different orders of magnitude.

The total data-misfit function $\Psi(\mathbf{m})$ is defined as the sum of the individual data-misfit functions (eq. 2) for each one of the $\alpha\beta$ -components of the gravity tensor, that is,

$$\begin{aligned}\Psi(\mathbf{m}) = & \psi^{xx}(\mathbf{m}) + \psi^{xy}(\mathbf{m}) + \psi^{xz}(\mathbf{m}) + \psi^{yy}(\mathbf{m}) \\ & + \psi^{yz}(\mathbf{m}) + \psi^{zz}(\mathbf{m}).\end{aligned}\quad (4)$$

The total data-misfit function given in eq. (4) holds when all components of the gravity-gradient tensor are considered. If some component is not considered, the practical procedure is to set up the respective normalizing factor (eq. 3) as zero. For example, if the xy - and yy -components are not considered, the interpreter must assign null values to the normalizing factors w^{xy} and w^{yy} (eq. 3).

The non-linear inverse problem of estimating the parameter vector \mathbf{m} that minimizes the total data-misfit function $\Psi(\mathbf{m})$ (eq. 4) is an ill-posed problem because the solution is neither unique nor stable. To transform this problem into a well-posed problem, we formulate a constrained non-linear inversion to obtain a 3-D shape of a geological body by minimizing

$$\Gamma(\mathbf{m}) = \Psi(\mathbf{m}) + \mu \sum_{\ell=1}^6 \alpha^\ell \phi^\ell(\mathbf{m}), \quad (5a)$$

subject to

$$m_{\min j} < m_j < m_{\max j}, \quad j = 1, \dots, M. \quad (5b)$$

In the inequality constraints (eq. 5b), the $m_{\min j}$ and $m_{\max j}$ are expressing the lower and upper bounds, respectively, to the j th element m_j of the parameter vector \mathbf{m} . These bounds ($m_{\min j}$ and $m_{\max j}$) both on the radii of all vertices of all prisms (r_j^k , $j = 1, \dots, M^k$, $k = 1, \dots, L$) and on the horizontal Cartesian coordinates of all arbitrary origins (x_0^k, y_0^k , $k = 1, \dots, L$) are defined element by element by the interpreter based on either the horizontal extent of the gravity gradient data or the geological knowledge about the studied area. In eq. 5(a), μ is the regularizing parameter and α^ℓ defines the weight of the ℓ th constraining function $\phi^\ell(\mathbf{m})$, $\ell = 1, \dots, 6$, proposed by Oliveira Jr. *et al.* (2011). These six constraining functions (from now on named constraints) are defined on parameter space as follows:

(1) $\phi^1(\mathbf{m})$: Smoothness constraint on the adjacent radii defining the horizontal section of each prism—This constraint imposes that adjacent radii within each prism must be close to each other. So, this constraint forces the estimated prisms to present a circular shape.

(2) $\phi^2(\mathbf{m})$: Smoothness constraint on the adjacent radii of adjacent prisms—This constraint imposes that adjacent radii within vertically adjacent prisms must be close to each other. Then, this constraint forces all estimated prisms to present a similar shape.

(3) $\phi^3(\mathbf{m})$: The source's outcrop constraint—In the case of outcropping sources, this constraint imposes that the estimated horizontal cross-section of the shallowest prism must be close to the known outcropping boundary.

(4) $\phi^4(\mathbf{m})$: The source's horizontal location constraint—In the case of outcropping sources, this constraint imposes that the estimated horizontal Cartesian coordinates of the arbitrary origin within the shallowest prism must be as close as possible to the known horizontal Cartesian coordinates of the outcropping portion of the source.

(5) $\phi^5(\mathbf{m})$: Smoothness constraint on the horizontal position of the arbitrary origins of adjacent prisms—This constraint imposes that the estimated horizontal Cartesian coordinates of vertically adjacent prisms must be close to each other. Hence, this constraint

forces smooth horizontal displacements between all vertically adjacent prisms.

(6) $\phi^6(\mathbf{m})$: Minimum Euclidian norm constraint on the adjacent radii within each prism—This constraint imposes that all estimated radii within each prism be close to null values.

Estimating the vector $\hat{\mathbf{m}}$ (the caret denotes estimate) by solving the constrained nonlinear inverse problem defined in eq. (5) is accomplished by Marquardt's (1963) method, incorporating the Gauss–Newton approximation of the Hessian matrices at each iteration. This algorithm is fully described in Silva *et al.* (2001) and Silva Dias *et al.* (2007) and the inequality constraints (eq. 5b) are introduced through a homeomorphic transformation (Barbosa *et al.* 1999). Finally, in order to improve the convergence of the non-linear optimization, we adopt a preconditioning strategy. This preconditioning is equivalent to multiply, at each iteration, the misfit functions $\psi^{\alpha\beta}(\mathbf{m})$ (eq. 2), $\alpha\beta = xx, xy, xz, yy, yz, zz$, by the ratio of the total number of parameters M to the trace of the Hessian matrix of the function $\|\mathbf{d}^{\alpha\beta}(\mathbf{m}) - \mathbf{g}^{\alpha\beta}\|_2^2$.

To obtain a stable solution which retrieves the shape of the source, we adopted the same practical procedure described in Oliveira Jr. *et al.* (2011). It follows that we obtain a set of Q estimates $\hat{\mathbf{m}}_1, \dots, \hat{\mathbf{m}}_Q$, each one estimated by inverting gravity-gradient observations corrupted with different Gaussian pseudo-random noise sequences with zero mean and a specified standard deviation. Then, we compute the sample mean vector $\tilde{\mathbf{m}}$ and the sample standard deviation vector $\tilde{\sigma}$. Here, $\tilde{\mathbf{m}}$ is an $M \times 1$ vector whose i th element \tilde{m}_i , $i = 1, \dots, M$, is the sample mean of a set of Q estimates of the i th elements of $\hat{\mathbf{m}}_k$, $k = 1, \dots, Q$, and $\tilde{\sigma}$ is an $M \times 1$ vector whose i th element $\tilde{\sigma}_i$, $i = 1, \dots, M$, is the sample standard deviation of a set Q estimates of the i th elements of $\hat{\mathbf{m}}_k$, $k = 1, \dots, Q$. The sample mean vector $\tilde{\mathbf{m}}$ is assumed to be a stable solution of the source's shape if all sample standard deviations ($\tilde{\sigma}_i$, $i = 1, \dots, M$) are smaller than an interpreter-specified value. This value depends on the noise level and (or) spatial distribution of the observations. In this work, we empirically established that the sample mean vector $\tilde{\mathbf{m}}$ is a stable solution of the source's shape if all sample standard deviations ($\tilde{\sigma}_i$, $i = 1, \dots, M$) are smaller than 4 per cent of its corresponding sample mean.

3 CRITERION FOR DETERMINING THE ESTIMATE HAVING THE OPTIMUM DEPTH TO THE BOTTOM

In Section 2, we established an interpretative model formed by an ensemble of L prisms (Fig. 1a), with a known density contrast and a constant and known thickness dz . The shallowest prism has the depth to the top equal to z_0 that presumably coincides with the top of the true geological source. These variables (L , dz and z_0) define the maximum depth to the bottom z_{\max} of the estimated body by

$$z_{\max} = z_0 + (L \cdot dz). \quad (6)$$

After setting up the interpretation model with a fixed depth to the bottom z_{\max} (eq. 6), our method obtains a stable estimate $\tilde{\mathbf{m}}$ of the 3-D shape of the source by applying the practical procedure described in Section 2. If the data have enough in-depth resolution, the method produces a stable estimate $\tilde{\mathbf{m}}$ that completely recovers the geometry of the true source and fits the data. Otherwise, the method can produce different stable estimates $\tilde{\mathbf{m}}$ that fit the data as well, each one with different depths z_{\max} for the interpretation model. To analyse the data resolution and overcome this non-uniqueness, we developed a new criterion for determining the best one among a set

of estimates having different maximum depths. This estimate can retrieve the true depth to the bottom of the source if the observed gravity-gradient data have enough in-depth resolution. Otherwise, the estimated source retrieves the minimum depth to the bottom required to recover the upper part of the source and to produce an acceptable data fit. This data-resolution analysis and the posterior choice of the estimate having the optimum maximum depth is done by new criterion based on the relationship between the estimated volume and the ℓ_2 -norm of the residuals produced by a set of estimated sources with different maximum depths.

This criterion for determining the optimum depth-to-bottom estimate of the source differs from the one developed by Oliveira Jr. *et al.* (2011) because the latter was deduced from Gauss' theorem and can be applied in gravity data only. By handling with gravity-gradient data, we cannot use Gauss' theorem, and thus we cannot use the Oliveira Jr. *et al.*'s (2011) criterion. Here, the new mathematical development of the criterion for determining the optimum depth-to-bottom estimate of the source makes it feasible to be applied not only to gravity-gradient data but also to multiple potential-field data (i.e. gravity, gravity-gradient, magnetic and magnetic-gradient data). In this way, this new criterion is more robust than the one developed by Oliveira Jr. *et al.* (2011).

3.1 Relationship between the predicted volume v_p and the ℓ_2 -norm s of the residuals

In this subsection, we present the theoretical relationship between the volume v_p of an estimated source (the predicted volume) and the ℓ_2 -norm s of the residuals between the observed and the predicted data. First, let $g_i^{\alpha\beta}$, $\alpha\beta = xx, xy, xz, yy, yz, zz$, be the $\alpha\beta$ -component of the gravity tensor field measured at the i th observation point (x_i, y_i, z_i) . Consider that $g_i^{\alpha\beta}$ is produced by a 3-D geological source located at subsurface, with constant density contrast ρ and defined by a volume v_0 (continuous black line in Fig. 2). Let us suppose that this geological source is approximated by an estimated homogeneous source with the same constant density contrast ρ and with a predicted volume v_p (dashed black line in Fig. 2). This approximation of the true geological source produces, at the same i th observation point, a predicted component of the gravity-gradient

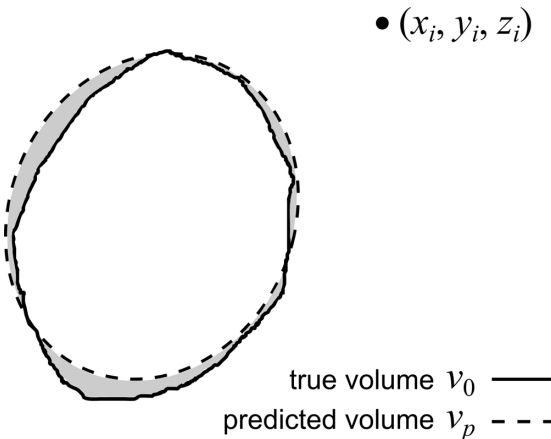


Figure 2. 2-D sketch of the true and predicted volumes. The gravity-gradient components produced by a homogeneous geological source with volume v_0 (continuous black line) are measured at the observation point (x_i, y_i, z_i) . The gravity-gradient components produced by a homogeneous estimated source with volume v_p (dashed black line) are computed at the same observation point (x_i, y_i, z_i) . The difference between the true (v_0) and the predicted (v_p) volumes is displayed as grey area.

tensor $d_i^{\alpha\beta}(v_p)$, $\alpha\beta = xx, xy, xz, yy, yz, zz$, that can be described by

$$d_i^{\alpha\beta}(v_p) = \rho \iiint_{v_p} G^{\alpha\beta}(\xi_i, \xi') dv, \quad (7)$$

where $G^{\alpha\beta}(\xi_i, \xi')$, $\alpha\beta = xx, xy, xz, yy, yz, zz$, is the Green's function associated with the $\alpha\beta$ -component of the gravity gradient tensor, ξ_i is the position vector of the i th observation point and the integration is conducted with respect to the variable ξ' denoting the position vector of an elementary volume inside v_p . By assuming that $g_i^{\alpha\beta} = d_i^{\alpha\beta}(v_0)$ and $v_p = v_0 + \Delta v$, where Δv (grey region in Fig. 2) is a small enough volume, then the predicted data $d_i^{\alpha\beta}(v_p)$ can be considered as an approximation of the observed data $g_i^{\alpha\beta}$. This approximation can be represented by a Taylor's expansion of first order about v_0 , leading to

$$\Delta d_i^{\alpha\beta} \approx \frac{d}{dv} d_i^{\alpha\beta}(v_0) \cdot (v_p - v_0), \quad (8)$$

where $\Delta d_i^{\alpha\beta} = d_i^{\alpha\beta}(v_p) - g_i^{\alpha\beta}$ and $\frac{d}{dv} d_i^{\alpha\beta}(v_0)$ is the first-order derivative of the $\alpha\beta$ -component of the gravity gradient tensor evaluated at v_0 . Eq. (8) shows that the linear relationship between $\Delta d_i^{\alpha\beta}$ and v_p , calculated at a fixed observation point (x_i, y_i, z_i) , depends on the derivative $\frac{d}{dv} d_i^{\alpha\beta}(v_0)$. If $\frac{d}{dv} d_i^{\alpha\beta}(v_0)$ is positive, the linear relationship between $\Delta d_i^{\alpha\beta}$ and v_p has a positive angular coefficient and vice versa. The relationship between $\Delta d_i^{\alpha\beta}$ and v_p can be illustrated by using the 2-D sketches shown in Fig. 3. In Fig. 3(a), the predicted data (dashed lines) represent a situation in which the predicted volume v_p is smaller than the true volume v_0 . In opposition, the predicted data shown in Fig. 3(b) (dashed lines) represent a situation in which the predicted volume v_p is greater than the true volume v_0 . Fig. 3(c) exemplifies the linear relationship between $\Delta d_i^{\alpha\beta}$ and v_p calculated at the position I of the 2-D sketches shown in Figs 3(a) and (b). Similarly, Fig. 3(d) exemplifies the linear relationship between $\Delta d_i^{\alpha\beta}$ and v_p calculated at the position II of the 2-D sketches shown in Figs 3(a) and (b). In Figs 3(c) and (d), the region A represents the situation illustrated in Fig. 3(a), where the volume v_p is smaller than the true volume v_0 . Conversely, the region B represents the situation illustrated in Fig. 3(b), where the volume v_p is greater than the true volume v_0 . This dependence of the signal of the angular coefficient of the linear relationship between v_p and $\Delta d_i^{\alpha\beta}$, calculated at the i th observation point (x_i, y_i, z_i) , disappears if we plot the predicted volume v_p against $(\Delta d_i^{\alpha\beta})^2$ (instead of $\Delta d_i^{\alpha\beta}$). The resulting curve is a parabola whose minimum $(\Delta d_i^{\alpha\beta})^2$ occurs when the predicted volume v_p is equal to the true volume v_0 (Fig. 3e). This is because by squaring both sides of eq. (8), we have

$$(\Delta d_i^{\alpha\beta})^2 \approx \beta_i^{\alpha\beta} (v_p - v_0)^2, \quad (9)$$

where $\beta_i^{\alpha\beta} = [\frac{d}{dv} d_i^{\alpha\beta}(v_0)]^2$. This equation shows that $(\Delta d_i^{\alpha\beta})^2 = 0$ at $v_p = v_0$ (Fig. 3e).

If we calculate, for each observation point (x_i, y_i, z_i) , $i = 1, \dots, N^{\alpha\beta}$, the $(\Delta d_i^{\alpha\beta})^2 \times v_p$ curve ($(\Delta d_i^{\alpha\beta})^2$ as function of v_p) by using eq. (9) and stack them, the resulting curve is still a parabola. This stack is equivalent to plot the predicted volume v_p against the ℓ_2 -norm of the residuals between the predicted data $d_i^{\alpha\beta}(v_p)$ and the observed gravity-gradient data $g_i^{\alpha\beta}$, $i = 1, \dots, N^{\alpha\beta}$. This norm can be given by

$$s^{\alpha\beta} = \frac{1}{N^{\alpha\beta}} \sum_{i=1}^{N^{\alpha\beta}} (\Delta d_i^{\alpha\beta})^2. \quad (10)$$

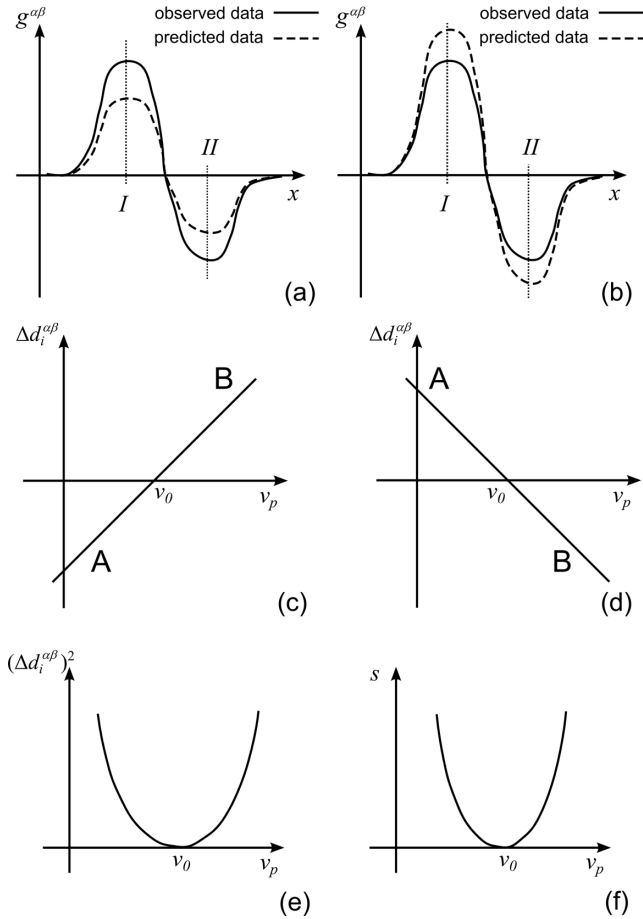


Figure 3. Sketches of the linear relationships and the parabolic shape of the $s \times v_p$ curve. The observed gravity-gradient component shown in (a) and (b) (solid line) is produced by a homogeneous geological source with volume v_0 . (a) Predicted gravity-gradient component (dashed line) produced by an estimated source with volume $v_p < v_0$. (b) Predicted gravity-gradient component (dashed line) produced by an estimated source with volume $v_p > v_0$. (c) and (d) show the linear relationship between $\Delta d_i^{\alpha\beta}$ and v_p calculated, respectively, at the positions I and II pinpointed in (a) and (b). The regions A and B displayed in (c) and (d) represent, respectively, the situations in which $v_p < v_0$ (a) and $v_p > v_0$ (b). (e) and (f) show, respectively, the $(\Delta d_i^{\alpha\beta})^2 \times v_p$ and the $s \times v_p$ curves calculated at an i th observation point. The characteristic parabolic shape of these curves does not depend on the position where they are calculated.

By substituting eq. (9) into eq. (10), we obtain

$$s^{\alpha\beta} \approx \hat{\beta}^{\alpha\beta} (v_p - v_0)^2, \quad (11)$$

where $\hat{\beta}^{\alpha\beta} = \left\{ \frac{1}{N^{\alpha\beta}} \sum_{i=1}^{N^{\alpha\beta}} \left[\frac{d}{dv} d_i^{\alpha\beta}(v_0) \right]^2 \right\}, \alpha\beta = xx, xy, xz, yy, yz, zz$.

Mathematically, eq. (11) is a parabola whose minimum ($s^{\alpha\beta} = 0$) occurs at $v_p = v_0$. In comparison with the $(\Delta d_i^{\alpha\beta})^2 \times v_p$ curve (eq. 9), which is calculated at a fixed observation point (x_i, y_i, z_i) , the $s^{\alpha\beta} \times v_p$ curve (eq. 11), with $s^{\alpha\beta}$ as a function of v_p , has a different curvature; however, the minimum $s^{\alpha\beta}$ still occurs when the predicted volume v_p is equal to the true volume v_0 .

By combining all components of the gravity tensor, we define the ℓ_2 -norm of the residuals between the observed and predicted

gravity-gradient data as

$$s = w^{xx} s^{xx} + w^{xy} s^{xy} + w^{xz} s^{xz} + w^{yy} s^{yy} + w^{yz} s^{yz} + w^{zz} s^{zz}, \quad (12)$$

where $w^{\alpha\beta}, \alpha\beta = xx, xy, xz, yy, yz, zz$, is given by eq. (3). Note that this ℓ_2 -norm (eq. 12) is equal to the total data-misfit function $\Psi(\mathbf{m})$ (eq. 4). Subsequently, by substituting the ℓ_2 -norm of the residuals $s^{\alpha\beta}$ (eq. 11) into eq. (12), we obtain

$$s \approx \hat{\beta} (v_p - v_0)^2, \quad (13)$$

where $\hat{\beta} = w^{xx} \hat{\beta}^{xx} + w^{xy} \hat{\beta}^{xy} + w^{xz} \hat{\beta}^{xz} + w^{yy} \hat{\beta}^{yy} + w^{yz} \hat{\beta}^{yz} + w^{zz} \hat{\beta}^{zz}$, with $\hat{\beta}^{\alpha\beta}, \alpha\beta = xx, xy, xz, yy, yz, zz$, being the curvatures in eq. (11). As pointed out before in Section 2, the normalizing factor $w^{\alpha\beta}$ is assigned a null value if the corresponding $\alpha\beta$ -component of the gravity gradient tensor is not used (or unavailable). In comparison with the $(\Delta d_i^{\alpha\beta})^2 \times v_p$ curve (eq. 9 and Fig. 3e) and the $s^{\alpha\beta} \times v_p$ curve (eq. 11), the $s \times v_p$ curve (eq. 13 and Fig. 3f) has a different curvature; however, the minimum s still occurs when the predicted volume v_p is equal to the true volume v_0 . The $s \times v_p$ curve (s as a function of v_p) is schematically illustrated in Fig. 3(f).

3.2 Relationship between the $s \times v_p$ curve and the depth to the bottom z_{\max} of the interpretation model and practical procedure for constructing the estimated $s \times v_p$ curve

Let us assume that the gravity tensor anomaly is caused by an isolated body with a constant density contrast with the host rocks and having a known depth to the top. In this case, we can expect that when z_{\max} is smaller than the true depth to the bottom of the source, the absolute values of the predicted gravity tensor data will underestimate the absolute values of the observed gravity tensor data (as shown in Fig. 3a). Conversely, if z_{\max} is greater than the true depth to the bottom of the source, the absolute values of predicted gravity tensor data will overestimate the absolute values of the observed gravity tensor data (as shown in Fig. 3b). Finally, if z_{\max} coincides with the true depth to the bottom of the source, the predicted gravity tensor data will be approximately equal to the observed gravity tensor data and a minimum value of the ℓ_2 -norm of the residuals s given in eq. (12) is expected. This minimum value of s is schematically shown in Fig. 3(f). In this way, by varying the thickness of all prisms forming the interpretation model (dz , in eq. 6), and consequently, varying the maximum depth to the bottom of the interpretation model (z_{\max} , in eq. 6), we construct an estimated $s \times v_p$ curve similar to the theoretical $s \times v_p$ curve (Fig. 3f). The tentative value for z_{\max} producing the smallest data-misfit measure s on the estimated $s \times v_p$ curve is an optimum estimate of the depth to the bottom of the source.

In practice, we compute the estimated $s \times v_p$ curve as follows. First, we establish the depth to the top z_0 , the number of prisms L , a small value for the thickness dz of all prisms and by using eq. (6), we calculate the depth to the bottom z_{\max} of the interpretation model. By assuming the correct density contrast ρ of the geological source, we estimate a stable parameter vector \mathbf{m} by using the proposed inverse method (eq. 5). Next, by using the $\alpha\beta$ -components, $\alpha\beta = xx, xy, xz, yy, yz, zz$, of the gravity-gradient tensor predicted by the estimated source, we compute the ℓ_2 -norm of the residuals s given in eq. (12). Finally, we plot s against the volume v_p of the estimated source, producing the first point of the estimated $s \times v_p$ curve. This procedure is repeated for increasingly larger values of the thickness dz of all prisms forming the interpretation model, and consequently, for increasingly larger values of bottom depth z_{\max} .

of the interpretation model. In practice, the estimated $s \times v_p$ curve does not have the perfect parabolic shape shown in Fig. 3(f). This departure of the estimated $s \times v_p$ curve from the theoretical $s \times v_p$ curve (eq. 13) can be attributed to (i) large differences between the predicted volume v_p and the true volume v_0 , which violates the Taylor's expansion described by eq. (8); (ii) the inadequacy of the interpretation model in retrieving the true geological body and then the estimated source does not fit acceptably the observed data; (iii) the presence of noise in the observed data and; (iv) the loss of in-depth resolution of the gravity-gradient data, which is inherent in the nature of potential-field data. Among these causes for the discrepancies between the estimated and theoretical $s \times v_p$ curves, the last one can be used in our favour for identifying if the data have enough in-depth resolution. If they do, the method can recover completely the geometry of the true source; otherwise,

the method produces an estimate having the minimum depth to the bottom required to fit the data. The practical use of the estimated $s \times v_p$ curve will be shown in synthetic tests.

4 APPLICATIONS TO SYNTHETIC DATA

4.1 Numerical validation of the estimated $s \times v_p$ curve for determining the true (or minimum) depth to the bottom of the source

To validate the theoretical behaviour of the $s \times v_p$ curve and its utility in completely retrieving the geometry of the true source, with correct source's bottom and volume, we computed the synthetic noise-free (not shown) and noise-corrupted data (grey scale maps in Fig. 4) of the xx -, xy -, xz -, yy -, yz - and zz -components of

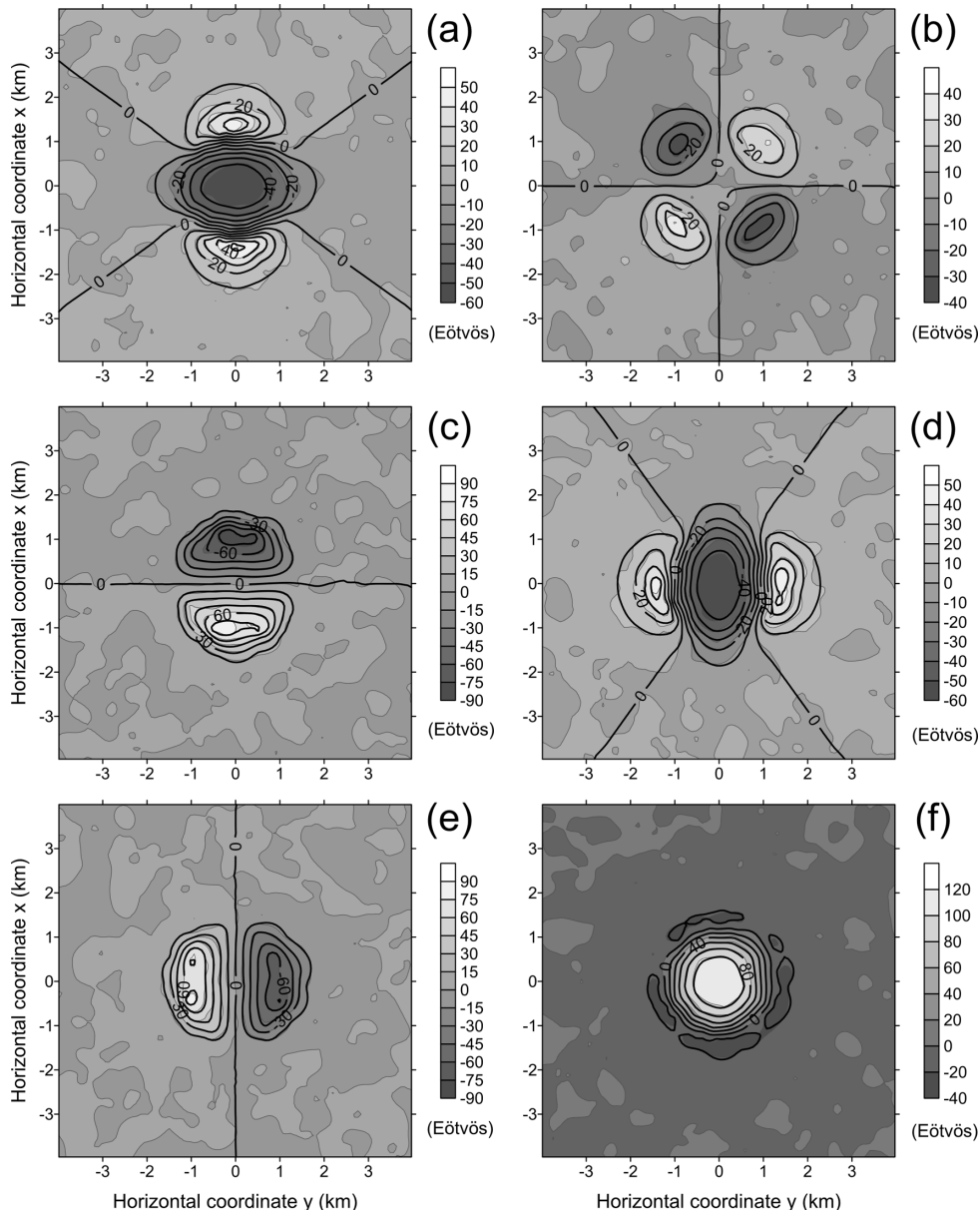


Figure 4. Synthetic noise-corrupted (grey scale maps) and predicted (black contour maps) (a) xx -, (b) xy -, (c) xz -, (d) yy -, (e) yz - and (f) zz -components of the gravity-gradient tensor. The synthetic components are produced by the simulated body shown in Fig. 5 (red prisms) and the predicted components are produced by the estimated body shown in Figs 5(b) and (c) (blue prisms).

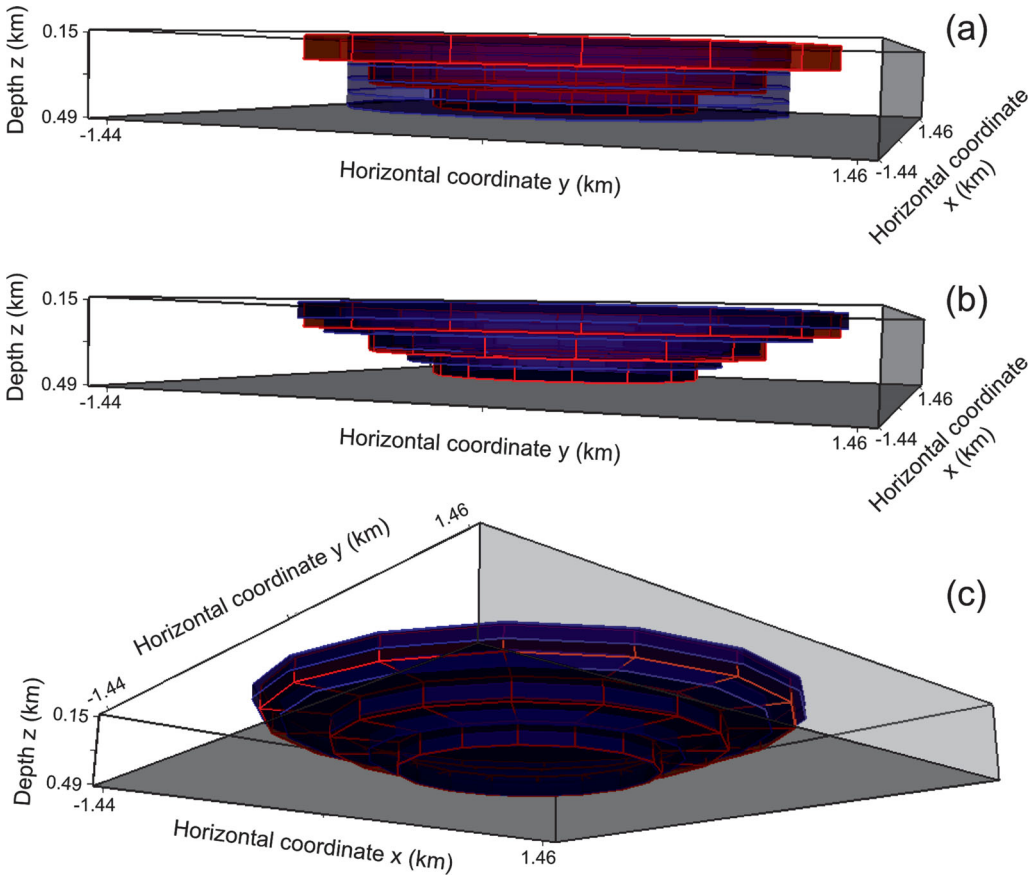


Figure 5. Perspective views of the simulated body (red prisms) with depth to the bottom of 450 m and volume of 0.8 km^3 . Perspective views in blue prisms of the (a) initial approximation, (b) and (c) estimated body. The estimated body in (b) and (c) is obtained by inverting the noise-corrupted data shown in Fig. 4 (grey scale maps) and assuming an interpretation model with depth to the bottom $z_{\max} = 450 \text{ m}$. The estimated body has a predicted volume $v_p = 0.8 \text{ km}^3$ and produces the predicted gravity gradient data shown in Fig. 4 (black contour maps).

the gravity-gradient tensor. In this test, each component contains $N^{\alpha\beta} = 681$, $\alpha\beta = xx, xy, xz, yy, yz, zz$, observations irregularly distributed on plane $z = 0 \text{ m}$. The synthetic data are corrupted with an uncorrelated pseudo-random Gaussian noise with zero mean and standard deviation of 3.0 Eötvös . These data are produced by a single homogeneous source with a density contrast ρ of 1.0 g cm^{-3} relative to the background and a volume of 0.8 km^3 (red prisms in Figs 5a–c). The source has maximum horizontal dimension of 2400 m and top and bottom at 150 and 450 m, respectively.

We applied the proposed inverse method to both synthetic noise-free (not shown) and noise-corrupted data (grey scale maps in Fig. 4). In both applications, we used an interpretation model formed by an ensemble of $L = 5$ prisms, all of them with the true density contrast $\rho^k = 1.0 \text{ g cm}^{-3}$ ($k = 1, \dots, 5$) and the same number of polygon vertices $M^k = 16$ ($k = 1, \dots, 5$), which describes the horizontal cross-sections. We also assumed the knowledge about the actual depth to the top of the simulated source; hence, we set the depth to the top of the interpretation model as $z_0 = 150 \text{ m}$. The five prisms which make up the initial approximation used in both applications have the same horizontal Cartesian coordinates of the arbitrary origins of $x_0^k = 0.0 \text{ m}$ and $y_0^k = 0.0 \text{ m}$ for all $k = 1, \dots, 5$. All vertices forming these prisms have the same radii $r_j^k = 1000 \text{ m}$, $j = 1, \dots, 16$, $k = 1, \dots, 5$.

By varying only the depth to the bottom z_{\max} of the interpretation model, we applied the proposed inverse method to the synthetic

noise-corrupted data (grey scale maps in Fig. 4) and produced five estimates. The value of z_{\max} varies from 350 to 550 m, in steps of 50 m, which lead to an uncertainty of $\pm 25 \text{ m}$ in the estimated depth to the bottom. We used all the constraining functions described in Section 2, except for the third and fourth constraints (named source's outcrop constraint and source's horizontal location constraint, respectively). In all these inversions, the lower and upper bounds for all radii forming all prisms of the interpretation model are 500 and 1300 m, respectively. Similarly, the lower and upper bounds for all horizontal Cartesian coordinates x_0^k and y_0^k , $k = 1, \dots, 5$, are -1000 and 1000 m , respectively. Figs 5(b) and (c) show perspective views of the estimated 3-D source (blue prisms) with $z_{\max} = 450 \text{ m}$, which produces the predicted components of the gravity-gradient tensor shown in Fig. 4 (black contour maps) and has a predicted volume v_p of 0.8 km^3 . The used initial approximation is shown in Fig. 5(a) (blue prisms). Each one of the five estimates obtained with the proposed method produces a ℓ_2 -norm of the residuals s (eq. 12) and a predicted volume v_p forming a point on the estimated $s \times v_p$ curve represented in Fig. 6 by open circles. On this curve, the estimated 3-D source shown in Fig. 5 is associated with the minimum s , which, in turn, is obtained by using a maximum depth $z_{\max} = 450 \text{ m}$ for the interpretation model. This estimated $s \times v_p$ curve (open circles in Fig. 6), which is obtained by inverting the noise-corrupted data (grey scale maps in Fig. 4), suggests that the proposed method can retrieve

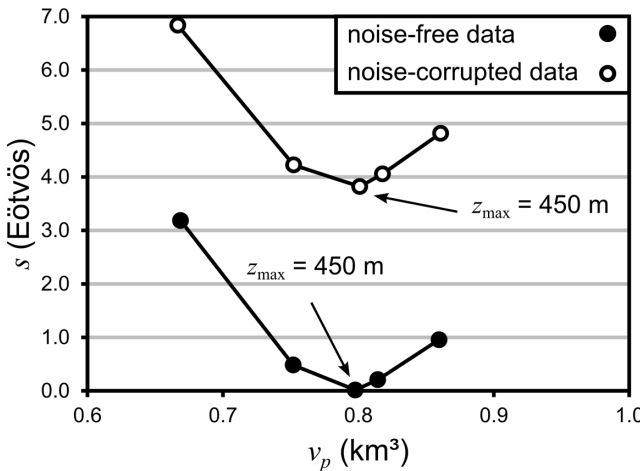


Figure 6. Estimated $s \times v_p$ curves obtained by inverting the noise-free (black dots) and noise-corrupted (open circles) data produced by the simulated body shown in Fig. 5 (red prisms). These curves are produced by varying the maximum depth to the bottom z_{\max} of the interpretation model from 350 m to 550 m, in steps of 50 m. The estimated body producing the well-defined minimum s on the $s \times v_p$ curve (open circles) obtained with the noise-corrupted data (grey scale maps in Fig. 4) is shown in Figs 5(b) and (c).

the geometry of the simulated source (red prisms in Fig. 5) completely. This fact is confirmed by Figs 5(b) and (c), which show two views of the estimated source (blue prisms) that retrieves the geometry of the simulated source (red prisms) completely. Note that in this synthetic test, the best depth-to-the-bottom (450 ± 25 m) and source volume (0.8 km^3) estimates are equal to the true ones.

By applying the proposed method to the noise-free data (not shown), we produced a similar $s \times v_p$ curve (black dots in Fig. 6) by varying the z_{\max} from 350 to 550 m, in steps of 50 m. Similarly to the estimated $s \times v_p$ curve obtained by using noise-corrupted data (open circles in Fig. 6), this curve (black dots in Fig. 6) exhibits a well-defined parabolic shape. The only difference is the dislocation along the s axis, showing the robustness of the method to the presence of noise. Likewise, the minimum of s on both estimated $s \times v_p$ curves (Fig. 6) are associated with $z_{\max} = 450$ m and volume $v_p = 0.8 \text{ km}^3$. The estimated sources (blue prisms) using the maximum depth $z_{\max} = 450$ m, for both noise-free (not shown) and noise-corrupted (Figs 5b and c) data, recover very well the geometry of the true simulated source (red prisms in Fig. 5).

Note that the estimated $s \times v_p$ curves obtained by using both noise-free data (black dots in Fig. 6) and noise-corrupted data (open circles in Fig. 6) confirm the quadratic relationship between the estimated source volume v_p and the ℓ_2 -norm of the residuals s , which were described in Section 3. Even considering the departure from $s = 0$ Eötvös caused by the presence of noise in data, these curves clearly show parabolic shapes whose minimum s occur when the bottom depth of the interpretation model coincides with the true depth to the bottom of the source. In this particular case, the consistency of the estimated $s \times v_p$ curves with the theoretical parabolic shape of the $s \times v_p$ curve can be attributed to the fact that we are dealing with an ideal synthetic test. This ideal test is characterized by the following factors: (1) the adequacy of the interpretation model to retrieve the simulated source and (2) the sufficient resolution of the gravity-gradient data set to resolve the simulated source.

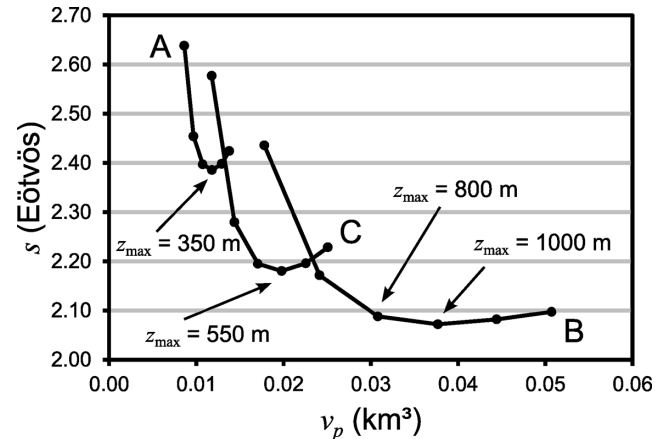


Figure 7. The estimated $s \times v_p$ curves A, B and C are obtained by inverting the noise-corrupted gravity-gradient data produced, respectively, by the simulated shallow-, deep- and intermediate-bottomed bodies (not shown). The well-defined minima s on the curves A and C disclose the enough resolution of the data sets to retrieve completely the simulated shallow (with depth to the bottom at 350 m and volume 0.012 km^3) and intermediate (with depth to the bottom at 550 m and volume 0.020 km^3) bottomed bodies, respectively. The ill-defined minimum s on the curve B discloses the insufficient resolution of the data set to retrieve completely the simulated deep-bottomed body (with depth to the bottom at 1000 m and volume 0.038 km^3).

These results confirm numerically the theoretical basis of the criterion for estimating not only a source having the *optimum* depth to the bottom, but also having the *optimum* volume, as described in Section 3. In both simulated cases (noise-free and noisy data), the estimated source producing the minimum s on the $s \times v_p$ curve (Fig. 6) has the depth to the bottom ($z_{\max} = 450 \pm 25$ m) and the volume ($v_p = 0.8 \text{ km}^3$) equal to the true ones.

To illustrate the utility of the $s \times v_p$ curve in recovering, at most, the lower-bound estimates of the source's depth to the bottom and of the source's volume, we simulated three synthetic gravity-gradient data sets (not shown). Each data set is produced by a single outcropping dipping source. Here, these three sources (not shown) have the same horizontal dimensions and the same physical property (density 1.0 g cm^{-3}). The only difference between them is the depth to the bottom. These three simulated sources are: shallow (with depth to the bottom at 350 m and volume 0.012 km^3), intermediate (with depth to the bottom at 550 m and volume 0.020 km^3) and deep (with depth to the bottom at 1000 m and volume 0.038 km^3) bottomed dipping sources. By inverting each data set, we obtain the estimated $s \times v_p$ curves A, B and C (Fig. 7). The well-defined minima of s on the $s \times v_p$ curves A and C (Fig. 7), which are produced, respectively, by the shallow- and intermediate-bottomed sources (not shown), reveal that the gravity-gradient data produced by these sources have enough resolution to estimate both the true depth to the bottom and the true volume of these simulated sources. In contrast, the $s \times v_p$ curve B (Fig. 7) produced by the deep-bottomed source (not shown) reveals multiple minima of s , which are associated with z_{\max} greater than or equal to 800 m. In this case, the estimated $s \times v_p$ curve B (Fig. 7) can be used to determine an estimated source having the minimum depth to the bottom ($z_{\max} = 800$ m) and the minimum volume ($v_p = 0.031 \text{ km}^3$) needed for producing an acceptable gravity-gradient data fit. Thus, the ill-defined minimum of s on the $s \times v_p$ curve B indicates that in comparison with the gravity-gradient data produced by the shallow- and intermediate-bottomed bodies, the

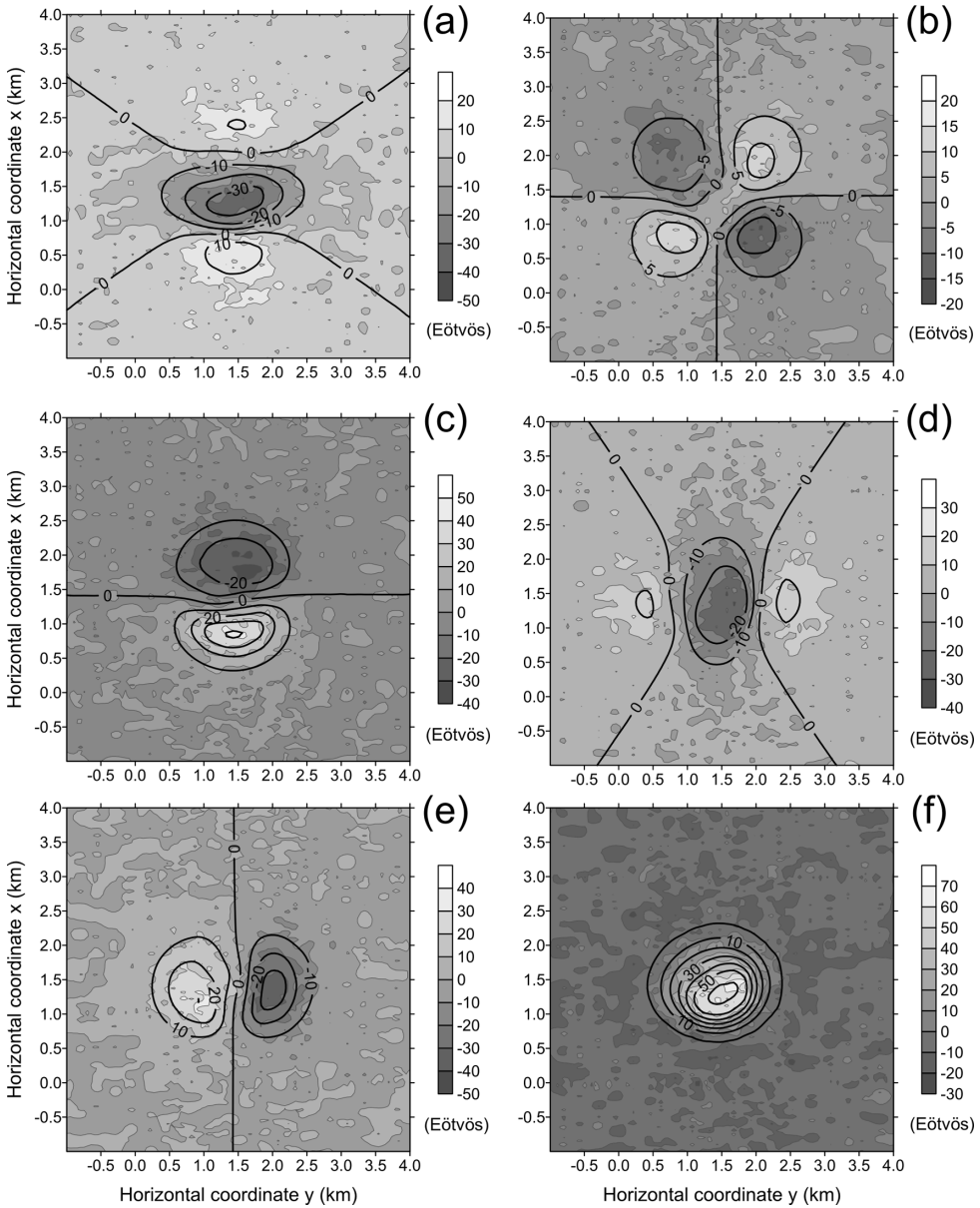


Figure 8. Synthetic noise-corrupted (grey scale maps) and predicted (black contour maps) (a) xx -, (b) xy -, (c) xz -, (d) yy -, (e) yz - and (f) zz -components of the gravity-gradient tensor. The synthetic components are produced by the simulated salt-dome cap rock shown in Fig. 9 (red wire-frame body). The predicted components are produced by the estimated body (blue prisms) shown in Figs 9(b) and (c).

gravity-gradient data produced by the deep-bottomed body do not have enough in-depth resolution. The estimated $s \times v_p$ curve B (Fig. 7) shows that it is not possible to retrieve the geometry of the deep-bottomed body at depths greater than 800 m. This result confirmed numerically that our criterion for determining the lower bounds for both the source's bottom and its volume, based on an ill-defined minimum value of s on the $s \times v_p$ curve, is sound.

We stress that all of the above results were obtained by assuming the knowledge about the depth to the top and density contrast of the simulated sources.

4.2 Simulating a real-world scenario

We computed the xx -, xy -, xz -, yy -, yz - and zz -noise-corrupted components of the gravity-gradient tensor (grey scale maps in

Fig. 8) produced by a synthetic body simulating a salt-dome cap rock. This simulated gravity-gradient survey follows the same flight pattern of an airborne gravity-gradient survey over the Vinton salt dome, USA (Ennen & Hall 2011). In this test, each component contains 3196 observations, totalling 19 176 measurements. To simulate experimental errors, each component of the gravity-gradient tensor is corrupted with an uncorrelated pseudo-random Gaussian noise with zero mean and a different standard deviation σ in Eötvös (Table 1). We also simulate systematic errors by shifting each component of the gravity-gradient tensor by a different constant b in Eötvös (Table 1). The simulated cap rock extends in depth from 160 to 460 m, with density contrast ρ of 0.55 g cm^{-3} and volume 0.366 km^3 (red wire-frame body in Fig. 9). The simulated body is based on an interpretation of the Vinton salt dome, reported by Ennen & Hall (2011).

Table 1. Test with synthetic data produced by a simulated salt-dome cap rock. Each component of the gravity-gradient tensor shown in Fig. 8 (grey scale maps) is corrupted with zero-mean Gaussian pseudo-random noise with a standard deviation σ , simulating experimental errors. Additionally, to each component of the gravity-gradient tensor is added a constant b , simulating systematic errors.

Gravity-gradient component	σ (Eötvös)	b (Eötvös)
xx	4.0	2.6
xy	2.5	0.1
xz	5.1	-2.0
yy	4.0	3.6
yz	4.7	-0.7
zz	6.8	-6.2

We applied our method by using an interpretation model formed by an ensemble of $L = 10$ prisms, all of them with the true density contrast $\rho^k = 0.55 \text{ g cm}^{-3}$ ($k = 1, \dots, 10$) and the same number of polygon vertices $M^k = 16$ ($k = 1, \dots, 10$), which describe the horizontal cross-sections of each polygon. We also assumed the knowledge about the actual depth to the top of the simulated source; hence, we set the depth to the top of the interpretation model as $z_0 = 160 \text{ m}$. The 10 prisms making up the initial approximation have the same horizontal Cartesian coordinates $x_0^k = 1150 \text{ m}$ and $y_0^k = 1606 \text{ m}$, $k = 1, \dots, 10$, of the arbitrary origins. The radii forming the shallowest prism (r_j^1 , $j = 1, \dots, 16$) are equal to 100 m; the radii forming the second prism (r_j^2 , $j = 1, \dots, 16$) are equal to 200 m. The sizes of radii of the third prism up to the 10th prism are increased successively by adding 100 m, until the radii of the deeper prism (r_j^{10} , $j = 1, \dots, 16$) attain 1000 m.

We construct the estimated $s \times v_p$ curve (Fig. 10) by producing 15 estimated sources, each one with a fixed maximum depth z_{\max} of the interpretation model. The z_{\max} varies from 320 to 580 m, in steps of 20 m leading to an uncertainty of $\pm 10 \text{ m}$ in the estimated

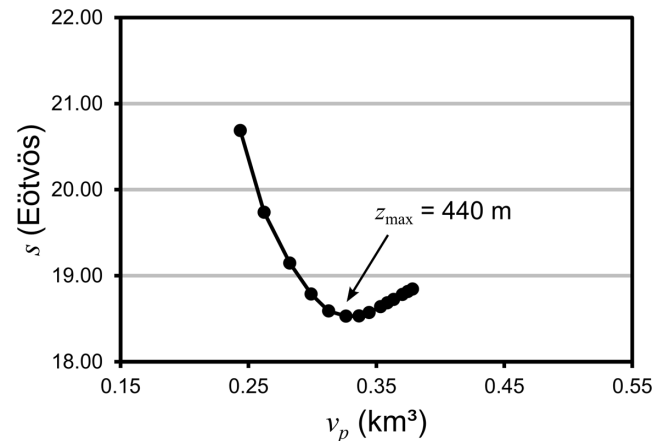


Figure 10. Estimated $s \times v_p$ curve obtained by inverting the noise-corrupted data (grey scale maps in Fig. 8) produced by the simulated salt dome cap rock shown in Fig. 9 (red wire-frame body). This curve is produced by varying the depth to the bottom z_{\max} of the interpretation model from 320 to 580 m, in steps of 20 m. The estimated body with $z_{\max} = 440 \text{ m}$ produces the well-defined minimum s on the estimated $s \times v_p$ curve and it is shown in Figs 9(b) and (c).

depth to the bottom. Each one of these eight estimates produces a pair of s and v_p (black dots in Fig. 10) on the estimated $s \times v_p$ curve. This curve presents a well-defined minimum of s , associated with $z_{\max} = 440 \text{ m}$ of the interpretation model. Fig. 9 shows the initial approximation (blue prisms in Fig. 9a) and two perspective views of the estimated salt-dome cap rock (blue prisms in Figs 9b and c) using the maximum depth $z_{\max} = 440 \text{ m}$ to set up the interpretation model. Although this estimated salt-dome cap rock is associated with a well-defined minimum of s on the estimated $s \times v_p$ curve (Fig. 10), it produces a predicted data (black contour maps in Fig. 8) that do not fit acceptably the noise-corrupted gravity-gradient data (grey scale maps in Fig. 8). This aspect is confirmed by the histograms (Fig. 11) of the residuals between the predicted (black

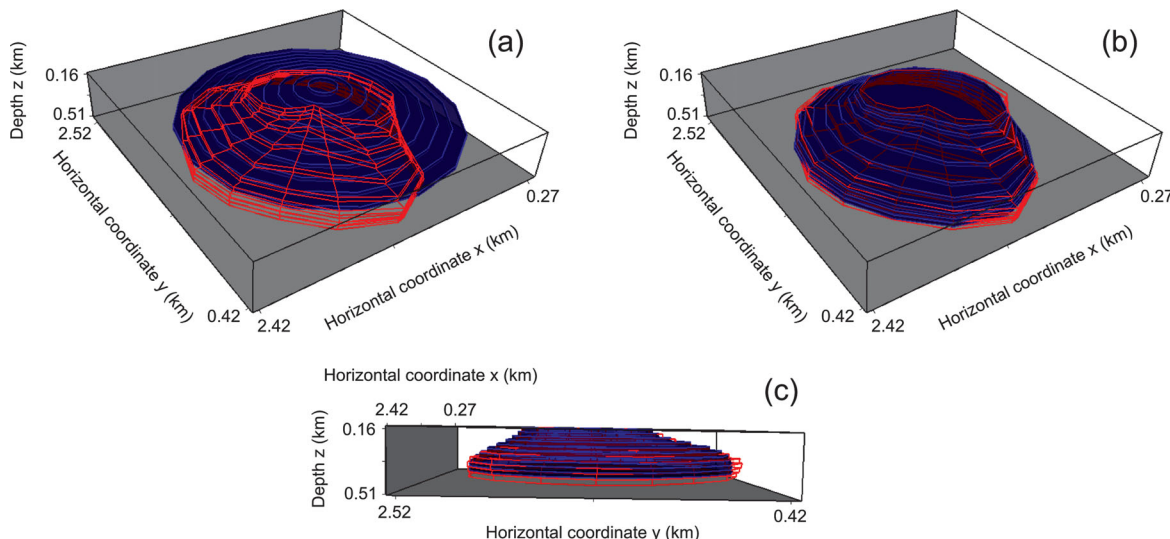


Figure 9. Perspective views of the simulated salt-dome cap rock (red wire-frame body) with depth to the bottom at 460 m and volume 0.372 km^3 . Perspective views in blue prisms of the (a) initial approximation, (b) and (c) estimated body. The estimated body in (b) and (c) is obtained by inverting the noise-corrupted data shown in Fig. 8 (grey scale maps) and assuming an interpretation model with depth to the bottom $z_{\max} = 440 \text{ m}$. The estimated body has a predicted volume $v_p = 0.337 \text{ km}^3$ and produces the predicted gravity-gradient data shown in Fig. 8 (black contour maps).

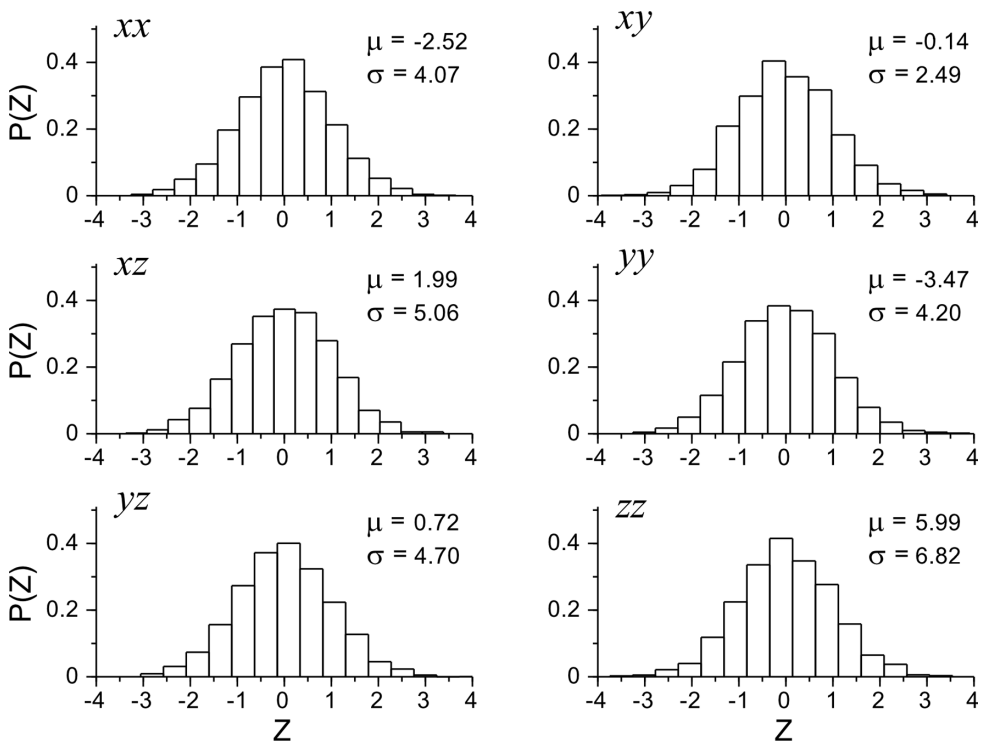


Figure 11. Histograms of the residuals between the predicted (black contour maps in Fig. 8) and the noise-corrupted (grey scale maps in Fig. 8) xx -, xy -, xz -, yy -, yz - and zz -components of the gravity-gradient tensor. The sample mean μ and the sample standard deviation σ are shown in each histogram. The residuals are transformed in a dimensionless variable Z by subtracting the residual value from the sample mean μ and then dividing the difference by the sample standard deviation σ . $P(Z)$ is the frequency curve of the variable Z .

contour maps in Fig. 8) and the simulated (grey scale maps in Fig. 8) noise-corrupted gravity-gradient data. These histograms resemble bell-shaped patterns indicating that the residuals of all components follow normal distributions. Moreover, the sample standard deviations σ calculated from the residuals (Fig. 11) are very close to the standard deviations σ (Table 1) of the noise realizations added to the synthetic data aiming at simulating experimental errors. However, the sample means μ calculated from the residuals (Fig. 11) are not close to zero, indicating that the predicted data do not fit the synthetic data. Note that the absolute values of these sample means μ (Fig. 11) are very close to the absolute values of the constants b (Table 1) that were added to the synthetic data simulating systematic errors. The most striking feature of these histograms (Fig. 11) is that they correctly characterize both the experimental and the systematic errors. Hence, by using these histograms, we can remove the systematic errors in the data. This correction consists in adding each sample non-zero mean μ calculated from the residuals (Fig. 11) to the corresponding component of the synthetic gravity-gradient data (grey scale maps in Fig. 8). This procedure leads to a new set of components of the gravity-gradient data shown in Fig. 12 (grey scale maps). By inverting these corrected gravity-gradient data, we recalculate the estimated $s \times v_p$ (Fig. 13). This new $s \times v_p$ curve shows a well-defined minimum of s associated with $z_{\max} = 460$ m of the interpretation model. Figs 14(b) and (c) show the perspective views of the estimated salt-dome cap rock (blue prisms) using the maximum depth $z_{\max} = 460$ m to set up the interpretation model. This estimate is obtained by using the initial approximation (blue prisms) shown in Fig. 14(a). Note that the estimated salt-dome cap rock (blue prisms in Figs 14b and c) completely retrieves the geometry of the simulated source (red wire-frame body shown in Figs 9

and 14), with the correct depth to the bottom ($z_{\max} = 460$ m) and a volume ($v_p = 0.372$ km³), which is very close to the true one (0.366 km³). The predicted data (black contour maps in Fig. 12) produced by this new estimated salt-dome cap rock fit acceptably the corrected gravity-gradient data (grey scale maps in Fig. 12). In contrast with the histograms shown in Fig. 11, the histograms of the residuals shown in Fig. 15 corroborate the acceptance of the data fitting. These histograms show sample means close to zero, indicating that the systematic errors were successfully removed from the data. These results show that our method is able to completely recover the geometry of a salt-dome cap rock, even in the presence of systematic errors in the data.

5 APPLICATION TO REAL DATA

We applied our method to interpret the full tensor gravity gradiometry (FTG) data acquired by Bell Geospace Inc. over the Vinton salt dome, at southwestern Louisiana, USA (grey scale maps in Fig. 16). The gravity-gradient data were terrain corrected using a density of 2.2 g cm⁻³ and each component contains 3196 observations, totalling 19 176. This salt dome is located in the onshore Gulf of Mexico, which is considered an important region producing oil and gas for more than one century (Coker *et al.* 2007). According to Coker *et al.* (2007), the Vinton salt dome is characterized by a massive cap rock extending above the salt rock. This cap rock is formed by gypsum and anhydrite which is embedded in sediments characterized by intercalated layers of sandstone and shale. Fig. 17 shows the density ranges of the principal rocks and minerals (Telford *et al.* 1990) present on the lithologies found in the

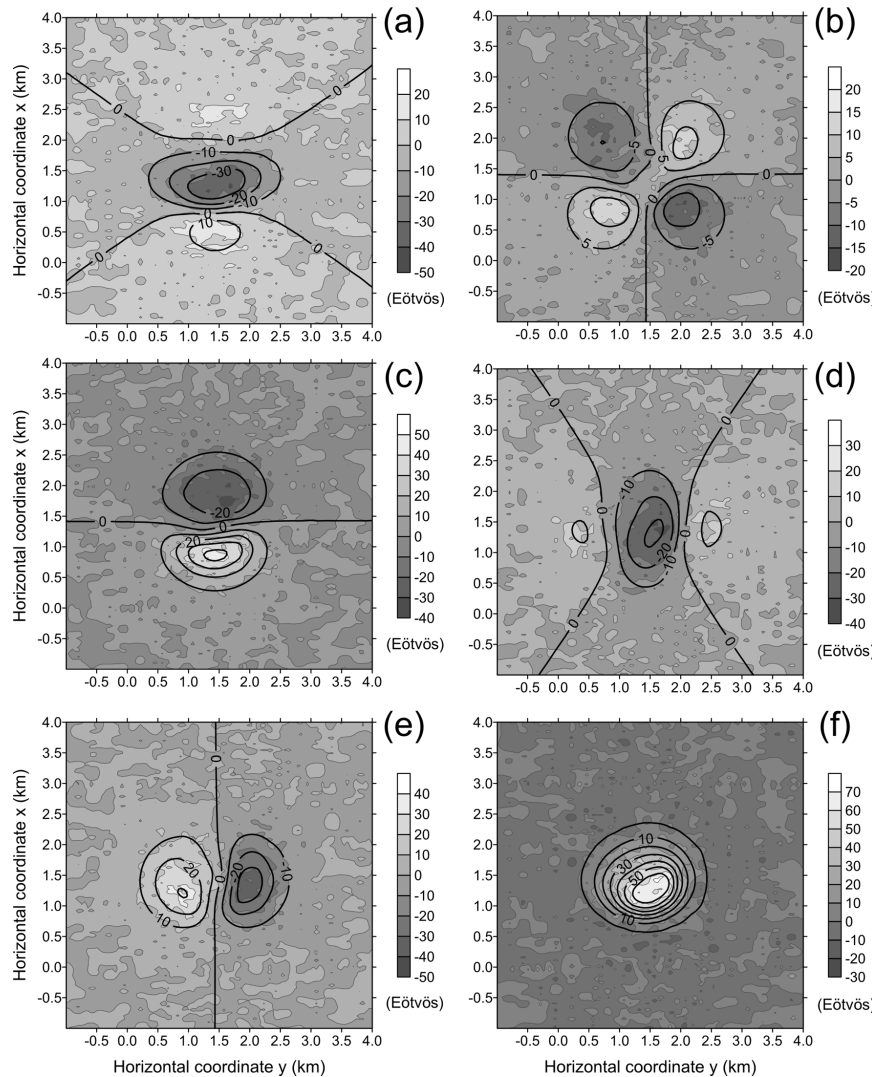


Figure 12. Synthetic noise-corrupted data (grey scale maps) corrected for the effect of systematic errors (Table 1) and predicted data (black contour maps) of the (a) xx -, (b) xy -, (c) xz -, (d) yy -, (e) yz - and (f) zz -components of the gravity-gradient tensor. The systematic errors are removed by adding the sample means of the residuals (μ in Fig. 11) to the original noise-corrupted data (grey scale maps in Fig. 8). The predicted components are produced by the estimated body (blue prisms) shown in Figs 14(b) and (c).

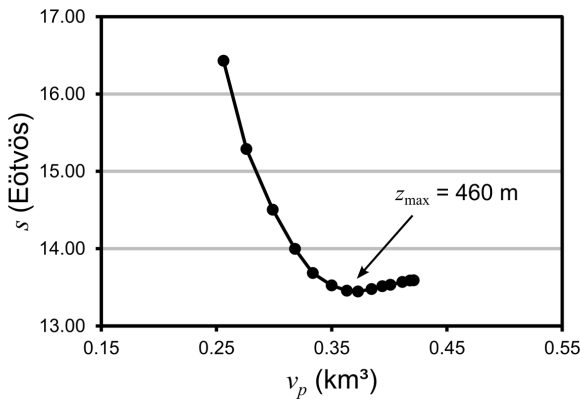


Figure 13. Estimated $s \times v_p$ curve obtained by inverting the corrected noise-corrupted data (grey scale maps in Fig. 12) produced by the simulated salt-dome cap rock (red wire-frame body in Figs 9 and 14). This curve is produced by varying the depth to the bottom z_{\max} of the interpretation model from 320 to 580 m, in steps of 20 m. The estimated body with $z_{\max} = 460$ m (blue prisms in Figs 14b and c) produces the well-defined minimum of s on the $s \times v_p$ curve.

study area. Following Ennen & Hall (2011), we assumed that the cap rock has a depth of the top at 160 m. Based on the density ranges of the lithologies (Fig. 17), we assumed that the surrounding sediments (shale and sandstone) and the salt dome have the same density 2.2 g cm^{-3} . This implies that the observed gravity-gradient data (grey scale maps in Fig. 16) are predominantly caused by the cap rock.

We applied our method to estimate the 3-D geometry of the cap rock. Based on Ennen & Hall (2011), we tested a geological hypothesis about the Vinton salt dome and adjacent rocks in which the cap rock has the density of 2.75 g cm^{-3} , resulting in a density contrast of 0.55 g cm^{-3} with the host rocks. Note that this possible density of the cap rock is within the density ranges shown in Fig. 17. To test this hypothesis, we applied our method by using an interpretation model with density contrast equal to 0.55 g cm^{-3} . The interpretation model is formed by an ensemble of $L = 10$ prisms, each one with the same number of polygon vertices $M^k = 16$ ($k = 1, \dots, 10$) describing the horizontal cross-sections of the polygons. Based on the prior information, we also assumed the knowledge about the actual depth to the top of the cap rock; hence, we set the depth to the top

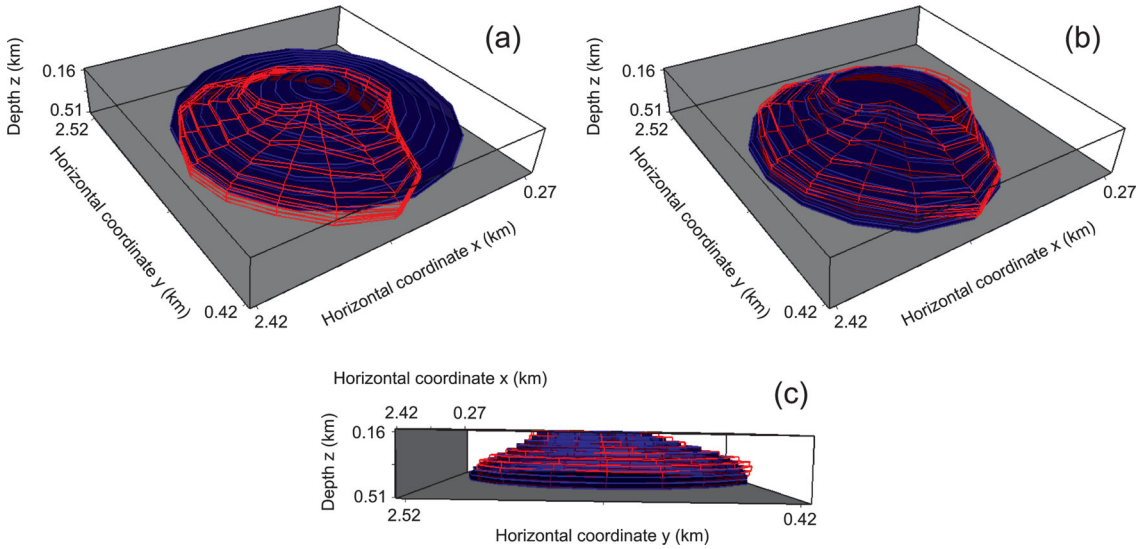


Figure 14. Perspective views of the simulated salt-dome cap rock (red wire-frame body) with depth to the bottom at 460 m and volume 0.366 km^3 . Perspective views in blue prisms of the (a) initial approximation, (b) and (c) estimated body. The estimated body in (b) and (c) is obtained by inverting the corrected noise-corrupted data (grey scale maps in Fig. 12) and assuming an interpretation model with depth to the bottom $z_{\max} = 460 \text{ m}$. The estimated body has a predicted volume $v_p = 0.372 \text{ km}^3$ and produces the predicted gravity-gradient data shown in Fig. 12 (black contour maps).

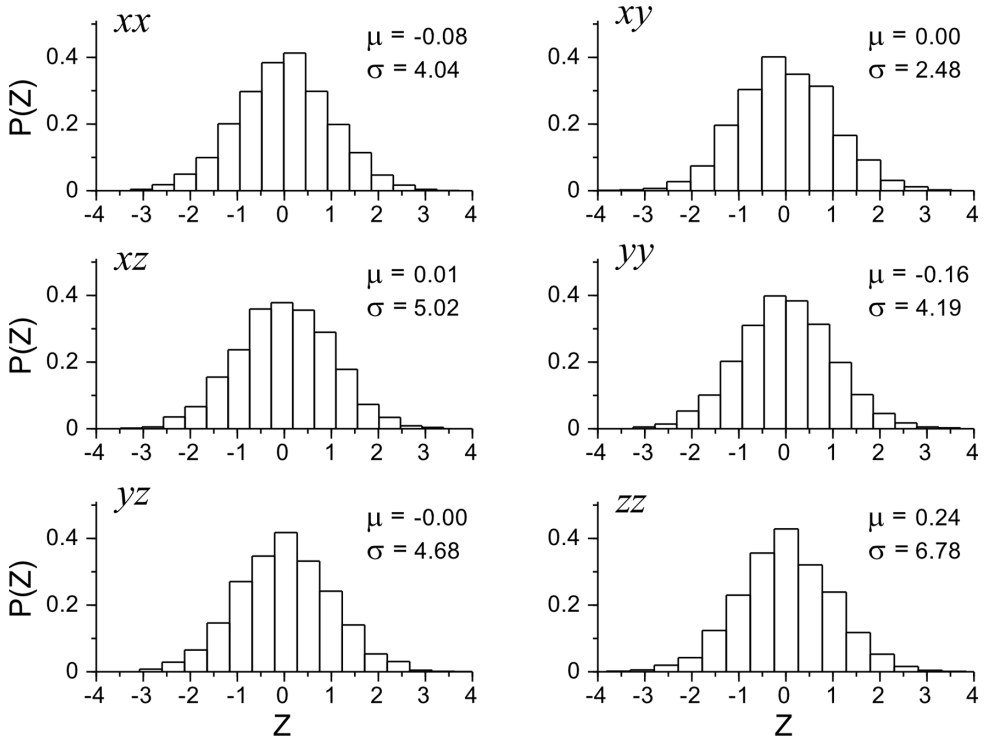


Figure 15. Histograms of the residuals between the predicted (black contour maps in Fig. 12) and the corrected noise-corrupted (grey scale maps in Fig. 12) xx -, xy -, xz -, yy -, yz - and zz -components of the gravity-gradient tensor. The sample mean μ and the sample standard deviation σ are shown in each histogram. The residuals are transformed in a dimensionless variable Z by subtracting the residual value from the sample mean μ and then dividing the difference by the sample standard deviation σ . $P(Z)$ is the frequency curve of the variable Z .

of the interpretation model as $z_0 = 160 \text{ m}$. The 10 prisms which make up the used initial approximation have the same horizontal Cartesian coordinates of $x_0^k = 3334.150 \text{ m}$ and $y_0^k = 442.606 \text{ m}$, $k = 1, \dots, 10$. Based on the synthetic application to interpret a simulated cap rock (Subsection 4.2), the radii forming the shallowest

prism (r_j^1 , $j = 1, \dots, 16$) are equal to 100 m and the radii forming the second prism (r_j^2 , $j = 1, \dots, 16$) are equal to 200 m. The sizes of radii of the third prism up to the 10th prism are increased successively by adding 100 m, until the radii of the deeper prism (r_j^{10} , $j = 1, \dots, 16$) attain 1000 m. We construct the estimated $s \times v_p$

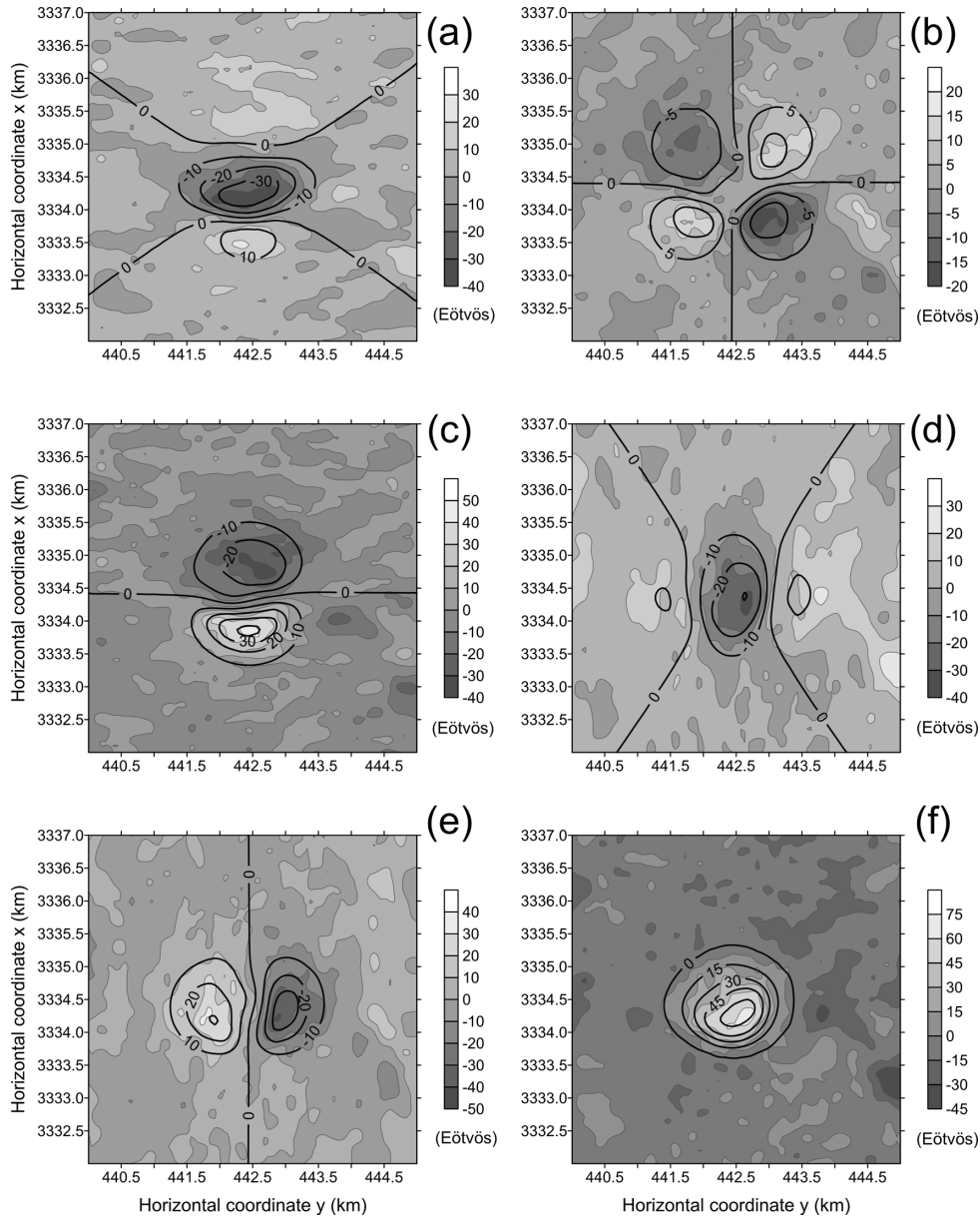


Figure 16. Interpretation of real data over the Vinton salt dome, USA. Observed (grey scale maps) and predicted (black contour maps) (a) xx -, (b) xy -, (c) xz -, (d) yy -, (e) yz - and (f) zz -components of the gravity-gradient tensor. The observed data are terrain corrected by using a density of 2.20 g cm^{-3} . The predicted data are produced by an estimated body (not shown).

curve (Fig. 18) using 14 pairs of s and v_p (black dots), each one produced by an estimated 3-D source with a different maximum depth to the bottom z_{\max} of the interpretation model. The value of z_{\max} varies from 320 to 580 m, in steps of 20 m, leading to an uncertainty of ± 10 m in the estimated depth to the bottom. The estimated $s \times v_p$ curve (Fig. 18) presents a well-defined minimum of s associated with an estimated 3-D cap rock (not shown) having maximum depth to the bottom $z_{\max} = 440$ m and a predicted volume $v_p = 0.327 \text{ km}^3$. This estimated 3-D cap rock (not shown) produces a predicted data (black contour maps in Fig. 16) that do not fit acceptably the observed gravity-gradient data (grey scale maps in Fig. 16). Similar to the results shown in the Subsection 4.2, the histograms (Fig. 19) of the residuals between the predicted and the observed gravity-gradient data confirm the unacceptable

data fittings, because the sample non-zero means μ (Fig. 19), which are calculated from the residuals. These non-zero means indicate the presence of systematic errors in the observed data (grey scale maps in Fig. 16). By adding each sample non-zero mean μ to the corresponding observed component of the gravity-gradient data (grey scale maps in Fig. 16), we produce corrected components of the gravity-gradient data (grey scale maps in Fig. 20). By inverting these corrected gravity-gradient data, we repeat the procedure for calculating a new estimated $s \times v_p$ curve (Fig. 21). This curve shows a well-defined minimum of s associated with $z_{\max} = 460$ m of the interpretation model. The estimated 3-D cap rock (Figs 22b and c) producing the minimum of s on the estimated $s \times v_p$ curve (Fig. 21) has a maximum depth $z_{\max} = 460$ m and a predicted volume $v_p = 0.366 \text{ km}^3$. Fig. 22(a) shows the initial approximation used in

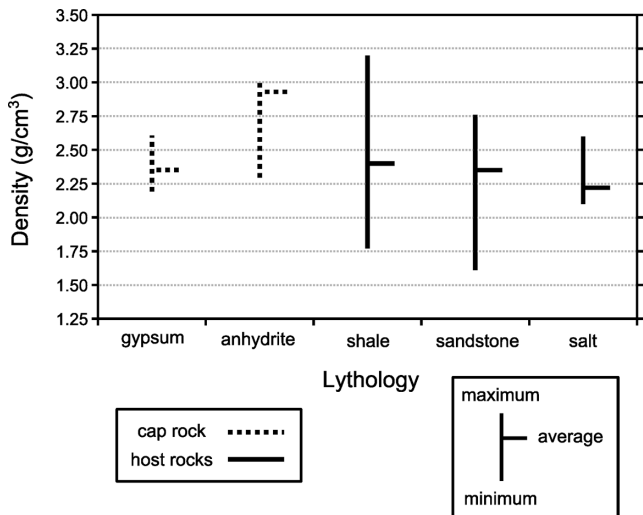


Figure 17. Interpretation of real data over the Vinton salt dome, USA. The graph shows the density ranges and the average values of the rock types and minerals according to Telford *et al.* (1990). These lithologies are identified in the study area as reported by Ennen & Hall (2011).

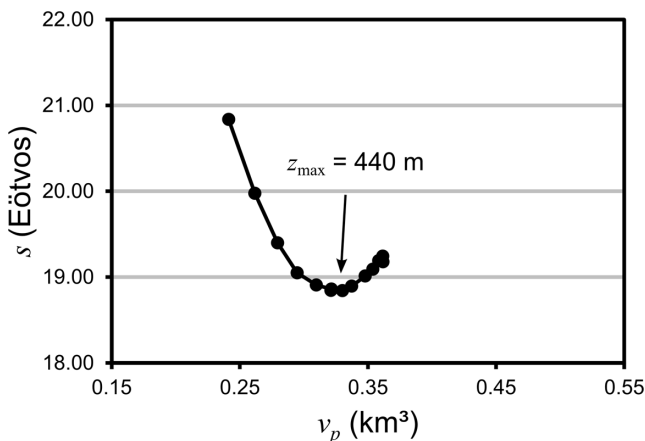


Figure 18. Interpretation of real data over the Vinton salt dome, USA. Estimated $s \times v_p$ curve obtained by inverting the real data shown in Fig. 16 (grey scale maps). This curve is constructed by varying the depth to the bottom z_{\max} of the interpretation model from 320 to 580 m, in steps of 20 m. The estimated body (not shown) producing the well-defined minimum of s on this $s \times v_p$ curve has a maximum depth to the bottom $z_{\max} = 440$ m and a predicted volume $v_p = 0.327 \text{ km}^3$.

this inversion. This 3-D estimated salt-dome cap rock (Figs 22b and c) yields acceptable data fittings, which is confirmed by the histograms of the residuals shown in Fig. 23. The predicted data (black contour maps) are shown in Fig. 20.

Note that the upper part of our estimated salt-dome cap rock (Figs 22b and c) has a northeast–southwest elongated form, being consistent with the strike of the main fault in the study area (Coker *et al.* 2007). We stress that this estimate represents a possible 3-D source that fits the observed gravity-gradient data over the Vinton salt dome, within the experimental errors. So, this estimate can be accepted as a possible geometry of the salt-dome cap rock. To confirm this estimated geometry, more prior geological

information about the Vinton salt dome and the surrounded rocks must be introduced.

6 CONCLUSIONS

We present a 3-D radial inversion of gravity-gradient data to estimate the shape of an isolated 3-D geological body, given its depth to the top and density contrast. We approximate the 3-D body by a set of vertically stacked right prisms with known thicknesses and density contrasts. Each prism has a polygonal horizontal cross-section whose vertices are described by polar coordinates referred to an origin within the polygon. By jointly inverting all gravity-gradient tensor components, we retrieve the shape of depth slices of the 3-D body by estimating the horizontal Cartesian coordinates of the origins and the radii of the vertices describing the horizontal cross-sections of all prisms. This estimate is formulated as a non-linear constrained inverse problem. By inverting the same gravity-gradient data set, our method can obtain different estimated bodies producing equally data fits but with different maximum depths. This ambiguity is a consequence of the inherent lack of in-depth resolution of potential-field data. To deal with this ambiguity and reduce the class of possible 3-D estimates compatible with the gravity-gradient data, we used a criterion based on the relationship between the ℓ_2 -norm of the residuals s and the volume v_p of different estimates obtained by using interpretation models with different maximum depths. The estimated v_p and s produced by each one of these estimates are plotted one against another, forming an estimated $s \times v_p$ curve. On this curve, the estimate producing the minimum s and fitting the gravity-gradient data is chosen as the *optimum* choice of the source's bottom depth. If the estimated $s \times v_p$ curve is a parabolic-shaped curve showing a well-defined minimum of s , the gravity-gradient data have sufficient resolution to recover the geometry of the 3-D geological body with both the correct volume and the correct maximum depth to the bottom. Otherwise, if the gravity-gradient data do not have enough resolution, the estimated $s \times v_p$ curve presents multiple minima of s produced by 3-D estimated source with different maximum depths. In this case, among these minima of s producing virtually the same data fit, the one associated with the minimum depth to the bottom of the source and producing an acceptable data fit is chosen as the *optimum* estimate.

By analyzing the histograms of the residuals, we show that our method is able to identify systematic errors and to correct the gravity-gradient data for these errors. If the corrected gravity-gradient data have sufficient resolution, our method obtains a stable estimate which recovers the geometry of the geological body completely.

In comparison with inverse methods that estimate the density-contrast distribution within a user-specified grid of 3-D right, juxtaposed prisms in the horizontal and vertical directions, our method is more computationally efficient because it does not require an intractable number of parameters and consequently does not deal with a large-scale 3-D inverse problem. Our method requires neither the use of depth-weighting functions adopted as a strategy to estimate sources at their correct depths nor the introduction of compactness and homogeneity constraints on the actual sources. On the other hand, our method is restricted to isolated bodies and assumes the knowledge about the correct

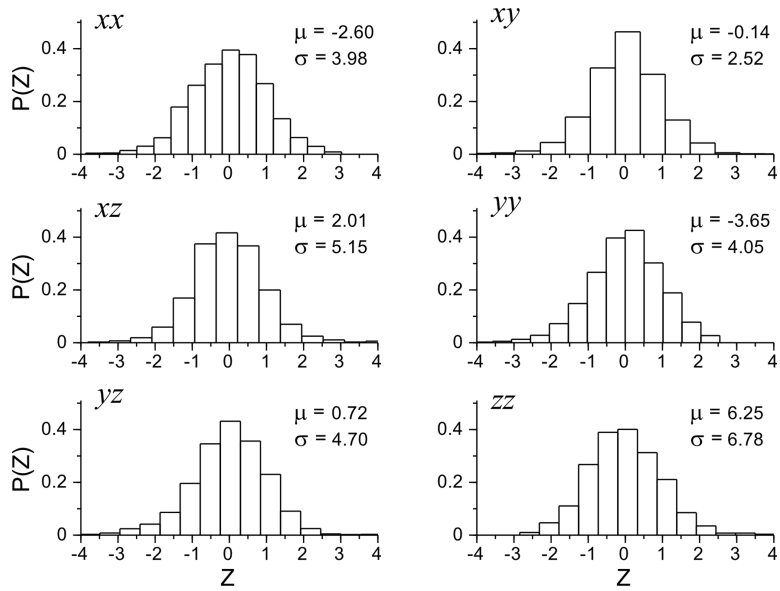


Figure 19. Interpretation of real data over the Vinton salt dome, USA. Histograms of the residuals between predicted (black contour maps in Fig. 16) and real (grey scale maps in Fig. 16) xx -, xy -, xz -, yy -, yz - and zz -components of the gravity-gradient tensor. The sample mean μ and the sample standard deviation σ are shown in each histogram. The residuals are transformed in a dimensionless variable Z by subtracting the residual value from the sample mean μ and then dividing the difference by the sample standard deviation σ . $P(Z)$ is the frequency curve of the variable Z .

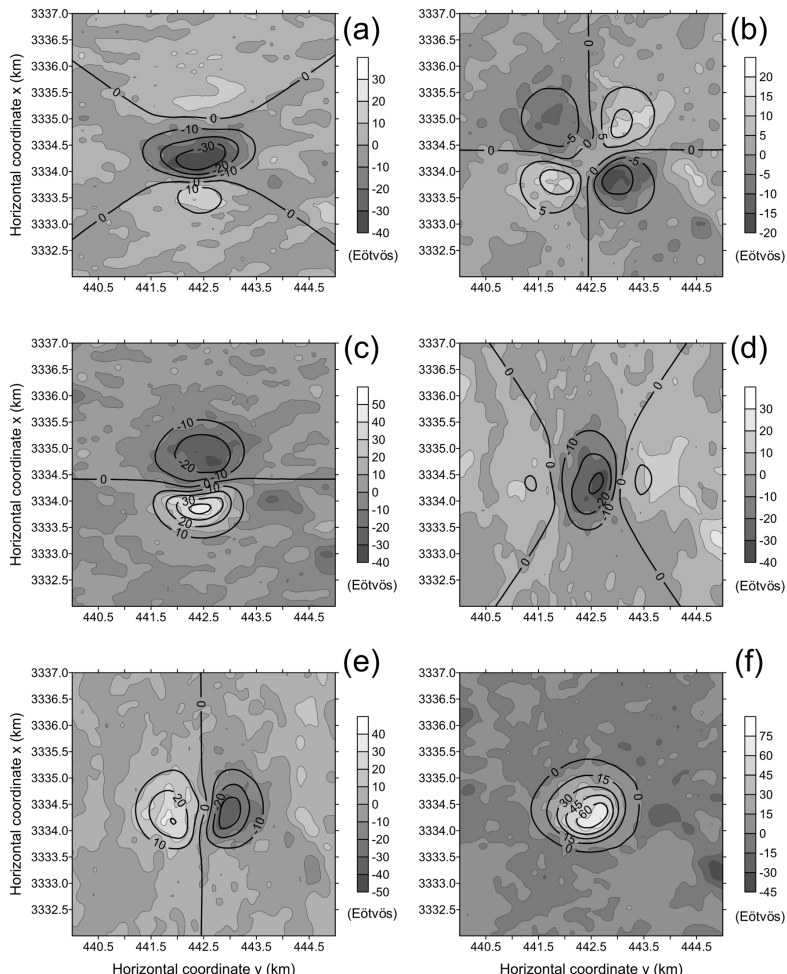


Figure 20. Interpretation of real data over the Vinton salt dome, USA. Real data (grey scale maps) corrected for the effect of systematic errors and predicted data (black contour maps) of the (a) xx -, (b) xy -, (c) xz -, (d) yy -, (e) yz - and (f) zz -components of the gravity-gradient tensor. The systematic errors are removed by adding the sample means of the residuals (μ in Fig. 19) to the original real data (grey scale maps in Fig. 16). The predicted components are produced by the estimated body (Figs 22b and c).

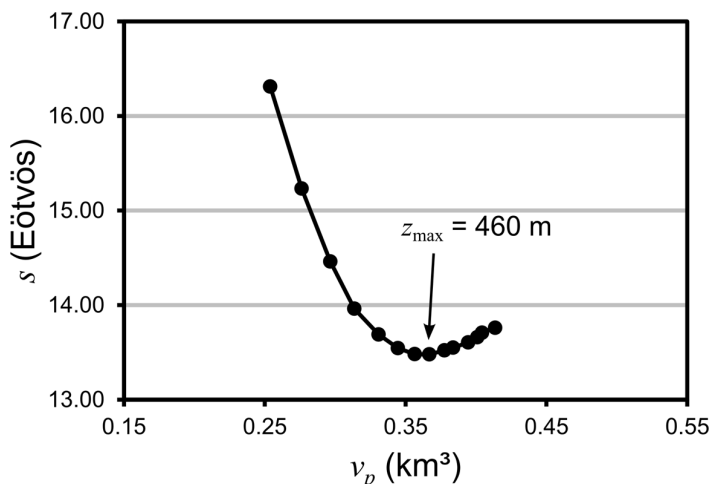


Figure 21. Interpretation of real data over the Vinton salt dome, USA. Estimated $s \times v_p$ curve obtained by inverting the corrected real data (grey scale maps in Fig. 20). This curve is constructed by varying the depth to the bottom z_{\max} of the interpretation model from 320 to 580 m, in steps of 20 m. The estimated body (Figs 22b and c) producing the well-defined minimum of s on this $s \times v_p$ curve has a maximum depth to the bottom $z_{\max} = 460$ m and a predicted volume $v_p = 0.366 \text{ km}^3$.

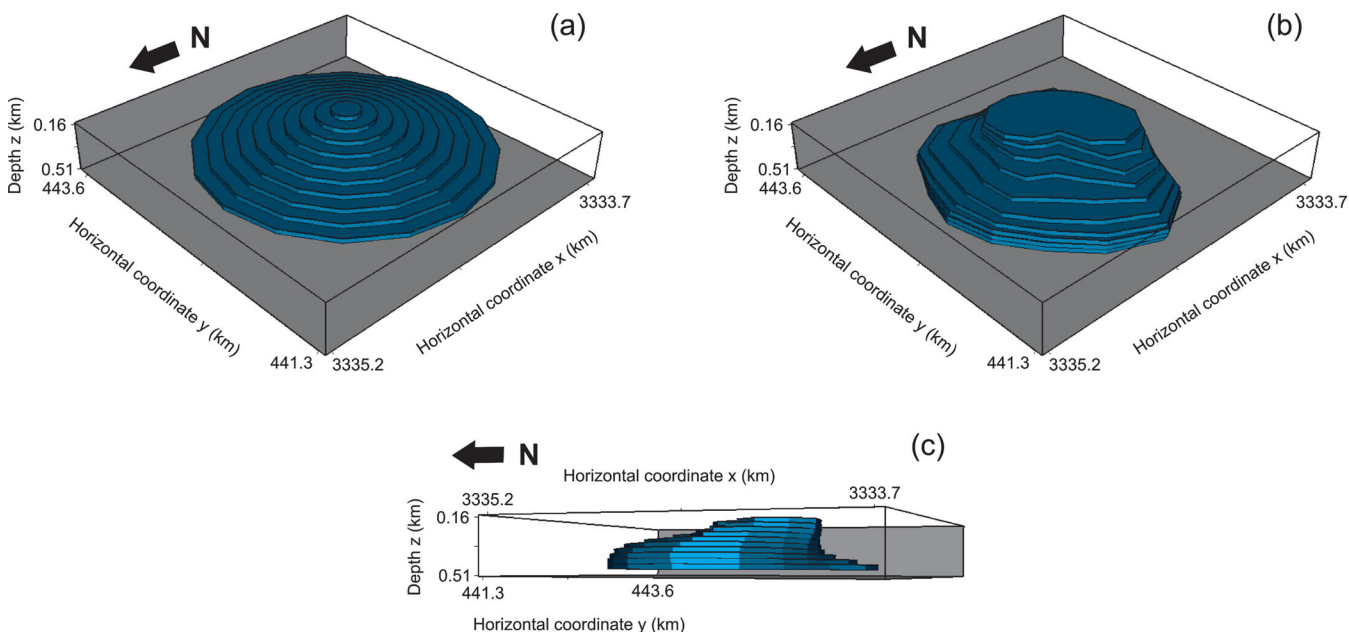


Figure 22. Interpretation of real data over the Vinton salt dome, USA. Perspective views of the (a) initial approximation, (b) and (c) estimated body. The estimated body in (b) and (c) is obtained by inverting the corrected real data (grey scale maps in Fig. 20) and assuming an interpretation model with depth to the bottom $z_{\max} = 460$ m. The estimated body has a predicted volume $v_p = 0.366 \text{ km}^3$ and produces the predicted gravity-gradient data shown in Fig. 20 (black contour maps).

depth of the top and density contrast of the 3-D geological body.

Our method can be extended, for example, to estimate the 3-D shape of multiple bodies producing interfering gravity-gradient anomalies, to perform a joint inversion of gravity and gravity-gradient data and to invert magnetic data. Additionally, in order to overcome problems with local minima, other optimization methods combining gradient-based algorithms and heuristic strategies could be employed.

ACKNOWLEDGEMENTS

We thank editor Bert Vermeersen and reviewer Fabio Caratori Tontini for their constructive comments and suggestions. We are particularly indebted to an anonymous reviewer for the criticisms and suggestions which improve the first version of the manuscript. The authors were supported in this research by a fellowship (V.C.F. Barbosa) and a scholarship (V.C. Oliveira Jr.) from Conselho Nacional de Desenvolvimento Científico e Tecnológico

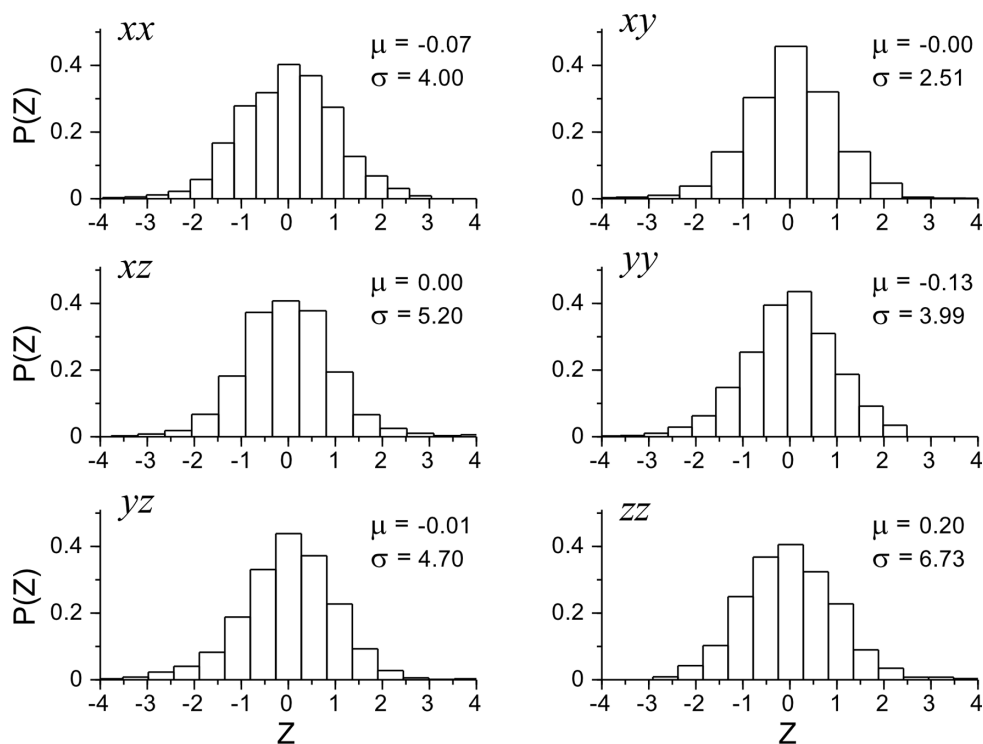


Figure 23. Interpretation of real data over the Vinton salt dome, USA. Histograms of the residuals between the predicted (black contour maps in Fig. 20) and the corrected real (grey scale maps in Fig. 20) xx -, xy -, xz -, yy -, yz - and zz -components of the gravity-gradient tensor. The sample mean μ and the sample standard deviation σ are shown in each histogram. The residuals are transformed in a dimensionless variable Z by subtracting the residual value from the sample mean μ and then dividing the difference by the sample standard deviation σ . $P(Z)$ is the frequency curve of the variable Z .

(CNPq), Brazil. Additional support for the authors was provided by the Brazilian research agencies CNPq (grant 471693/2011-1) and FAPERJ (grant E-26/103.175/2011). The authors thank Bell Geospace Inc. for permission to use the real data from the Vinton salt dome.

REFERENCES

- Barbosa, V.C.F. & Silva, J.B.C., 1994. Generalized compact gravity inversion, *Geophysics*, **59**, 57–68.
- Barbosa, V.C.F. & Silva, J.B.C., 2011. Reconstruction of geologic bodies in depth associated with a sedimentary basin using gravity and magnetic data, *Geophys. Prospect.*, **59**, 1021–1034.
- Barbosa, V.C.F., Silva, J.B.C. & Medeiros, W.E., 1997. Gravity inversion of basement relief using approximate equality constraints on depths, *Geophysics*, **62**, 1745–1757.
- Barbosa, V.C.F., Silva, J.B.C. & Medeiros, W.E., 1999. Gravity inversion of a discontinuous relief stabilized by weighted smoothness constraints on depth, *Geophysics*, **64**, 1429–1437.
- Barnes, G. & Barraud, J., 2012. Imaging geologic surfaces by inverting gravity gradient data with depth horizons, *Geophysics*, **77**, G1–G11.
- Beiki, M. & Pedersen, L.B., 2010. Eigenvector analysis of gravity gradient tensor to locate geologic bodies, *Geophysics*, **75**, I37–I49.
- Bertete-Aguirre, H., Cherkaev, E. & Oristaglio, M., 2002. Non-smooth gravity problem with total variation penalization functional, *Geophys. J. Int.*, **149**, 499–507.
- Caratori-Tontini, F., Cocchi, L. & Carmisciano, C., 2009. Rapid 3-D forward model of potential fields with application to the Palinuro seamount magnetic anomaly (southern Tyrrhenian Sea, Italy), *J. geophys. Res.*, **114**, B02103.
- Coker, M.O., Bhattacharya, J.P. & Marfurt, K.J., 2007. Fracture patterns within mudstones on the flanks of a salt dome: syneresis or slumping? *Gulf Coast Assoc. geol. Soc. Trans.*, **57**, 125–137.
- Ditmar, P., 2002. Finding the shape of a local heterogeneity by means of a structural inversion with constraints, *Geophys. Prospect.*, **50**, 209–223.
- Ennen, C. & Hall, S., 2011. Structural mapping of the Vinton salt dome, Louisiana, using gravity gradiometry data, in *Proceedings of SEG Annual Meeting, SEG International Exposition and 83rd Annual Meeting*, San Antonio, 18–23 September 2011, SEG.
- Farquharson, C.G., 2008. Constructing piecewise-constant models in multidimensional minimum-structure inversions, *Geophysics*, **73**, K1–K9.
- Fregoso, E. & Gallardo, L.A., 2009. Cross-gradients joint 3-D inversion with applications to gravity and magnetic data, *Geophysics*, **74**, L31–L42.
- Gordon, A.C., Mohriak, W.U. & Barbosa, V.C.F., 2012. Crustal architecture of the Almada Basin, NE Brazil: an example of a non-volcanic rift segment of the South Atlantic passive margin, in *Conjugate Divergent Margins*, Vol. 369, pp. 215–234, eds Mohriak, W.U., Danforth, A., Post, P.J., Brown, D.E., Tari, G.C., Nemcok, M. & Sinha, S.T., Geological Society London Special Publications.
- Guillen, A. & Menichetti, V., 1984. Gravity and magnetic inversion with minimization of a specific functional, *Geophysics*, **49**, 1354–1360.
- Guspi, F., 1993. Noniterative nonlinear gravity inversion, *Geophysics*, **58**, 935–940.
- Last, B.J. & Kubik, K., 1983. Compact gravity inversion, *Geophysics*, **48**, 713–721.
- Lelièvre, P.G. & Oldenburg, D.W., 2009. A comprehensive study of including structural orientation information in geophysical inversions, *Geophys. J. Int.*, **178**, 623–637.
- Li, Y., 2001. 3-D inversion of gravity gradiometer data, in *Proceedings of the 71st Annual International Meeting*, SEG, Expanded Abstracts, pp. 1470–1473.
- Li, Y. & Oldenburg, D.W., 1998. 3-D inversion of gravity data, *Geophysics*, **63**, 109–119.
- Luo, X., 2010. Constraining the shape of a gravity anomalous body using reversible jump Markov chain Monte Carlo, *Geophys. J. Int.*, **180**, 1067–1089.
- Marquardt, D.W., 1963. An algorithm for least-squares estimation of nonlinear parameters, *J. Soc. Ind. appl. Math.*, **2**, 601–612.

- Martins, C.M., Barbosa, V.C.F. & Silva, J.B.C., 2010. Simultaneous 3-D depth-to-basement and density-contrast estimates using gravity data and depth control at few points, *Geophysics*, **75**, I21–I28.
- Martins, C.M., Lima, W.A., Barbosa, V.C.F. & Silva, J.B.C., 2011. Total variation regularization for depth-to-basement estimate: part 1 – mathematical details and applications, *Geophysics*, **76**, I1–I12.
- Mikhailov, V., Pajot, G., Diamant, M. & Price, A., 2007. Tensor deconvolution: a method to locate equivalent sources from full tensor gravity data, *Geophysics*, **72**, I61–I69.
- Moraes, R.A.V. & Hansen, R.O., 2001. Constrained inversion of gravity fields for complex 3-D structures, *Geophysics*, **66**, 501–510.
- Oezsen, R., 2004. Velocity modelling and prestack depth imaging below complex salt structures: a case history from on-shore Germany, *Geophys. Prospect.*, **52**, 693–70.
- Oliveira, Jr., V.C., Barbosa, V.C.F. & Silva, J.B.C., 2011. Source geometry estimation using the mass excess criterion to constrain 3-D radial inversion of gravity data, *Geophys. J. Int.*, **187**, 754–772.
- Parker, R.L., 1973. The rapid calculation of potential anomalies, *Geophys. J. Roy. astr. Soc.*, **31**, 447–455.
- Plouff, D., 1976. Gravity and magnetic fields of polygonal prisms and application to magnetic terrain corrections, *Geophysics*, **41**, 727–741.
- Portniaguine, O. & Zhdanov, M.S., 1999. Focusing geophysical inversion images, *Geophysics*, **64**, 874–887.
- Richardson, M.R. & MacInnes, S.C., 1989. The inversion of gravity data into three-dimensional polyhedral models, *J. geophys. Res.*, **94**, 7555–7562.
- Silva, J.B.C. & Barbosa, V.C.F., 2004. Generalized radial inversion of 2D potential field data, *Geophysics*, **69**, 1405–1413.
- Silva, J.B.C. & Barbosa, V.C.F., 2006. Interactive gravity inversion, *Geophysics*, **71**, J1–J9.
- Silva, J.B.C., Costa, D.C.L. & Barbosa, V.C.F., 2006. Gravity inversion of basement relief and estimation of density contrast variation with depth, *Geophysics*, **71**, J51–J58.
- Silva, J.B.C., Medeiros, W.E. & Barbosa, V.C.F., 2000. Gravity inversion using convexity constraint, *Geophysics*, **65**, 102–112.
- Silva, J.B.C., Medeiros, W.E. & Barbosa, V.C.F., 2001. Pitfalls in nonlinear inversion, *Pure appl. Geophys.*, **158**, 945–964.
- Silva, J.B.C., Oliveira, A.S. & Barbosa, V.C.F., 2010. Gravity inversion of 2D basement relief using entropic regularization, *Geophysics*, **75**, I29–I35.
- Silva Dias, F.J.S., Barbosa, V.C.F. & Silva, J.B.C., 2007. 2D gravity inversion of a complex interface in the presence of interfering sources, *Geophysics*, **72**, I13–I22.
- Silva Dias, F.J.S., Barbosa, V.C.F. & Silva, J.B.C., 2009. 3-D gravity inversion through an adaptive learning procedure, *Geophysics*, **74**, I9–I21.
- Silva Dias, F.J.S., Barbosa, V.C.F. & Silva, J.B.C., 2011. Adaptive learning 3-D gravity inversion for salt-body imaging, *Geophysics*, **76**, I49–I57.
- Telford, W.M., Geldart, L.P. & Sheriff, R.E., 1990. *Applied Geophysics*, Cambridge University Press.
- Uieda, L. & Barbosa, V.C.F., 2012. Robust 3-D gravity gradient inversion by planting anomalous densities, *Geophysics*, **77**, G55–G66.
- Wildman, R.A. & Gazonas, G.A., 2009. Gravitational and magnetic anomaly inversion using a tree-based geometry representation, *Geophysics*, **74**, I23–I35.
- Zhang, C., Mushayandebvu, M.F., Reid, A.B., Fairhead, J.D. & Odegard, M.E., 2000. Euler deconvolution of gravity tensor gradient data, *Geophysics*, **65**, 512–520.
- Zhdanov, M.S., Ellis, R. & Mukherjee, S., 2004. Three-dimensional regularized focusing inversion of gravity gradient tensor component data, *Geophysics*, **69**, 925–937.

SUPPORTING INFORMATION

Additional Supporting Information may be found in the online version of this article:

Supporting Information for ‘3-D radial gravity gradient inversion’ (<http://gji.oxfordjournals.org/lookup/suppl/doi:10.1093/gji/ggt307/-/DC1>)

Please note: Oxford University Press are not responsible for the content or functionality of any supporting materials supplied by the authors. Any queries (other than missing material) should be directed to the corresponding author for the article.